

修士学位論文

Research on Dielectric Waveguides for
Enhancing Spatial Resolution in Beyond 5G
High Frequency Communications

Beyond 5G 高周波通信の空間分解能を向上
するための誘電体導波路の研究

2023年1月6日提出
総合分析情報学コース
指導教員 中尾彰宏 教授
49-216421
三谷 恵司

Abstract

With the rapid development of communication technology, the demand for antennas and cables, essential components for signal processing, is growing by leaps and bounds. In addition, demand for mmWave antennas and cables are increasing as components for specific bands are necessary for individual merchants to build their own Local 5G base stations.

However, components such as antennas and cables used currently need certain processing costs and processing time, increasing the complexity and spectral characteristics and creating limitations in the design and implementation. Moreover, it takes more time and expense for specific antennas and cables because of their particular characteristics. Furthermore, infrastructure created by traditional components is often irreversible, and cannot be changed once the components are set in position. This is acceptable for a small number of network areas, but if the number of local networks is large and the architecture is complex, this leads to interference between wireless signals. For this reason, we propose to design and produce mmWave antennas using dielectric waveguides to reduce the cost, processing time and create a distributive local area network.

This paper designs mainly three kinds of dielectric waveguide antenna and details the design process and simulation process. First, we introduce the related background and how Maxwell's electromagnetic equations tie into the characteristics of dielectric waveguides. Then we describe the basic theory of the antenna's design, and simulate them on a simulator. After the structure and order are determined first, we iterate the simulation until the S-parameters and half-power beam width are optimized. After assembling the dielectric waveguide antenna, we observe the actual test results and demonstrate the feasibility using the scalar network analyzer and vector network analyzer.

The implemented antennas shows the antenna functions with less than 10dB insertion loss and around 20 degrees of half-power beamwidth. The proposed implementation method can effectively reduce the machining time within 1 day due to the simple principle and the procedural process. Furthermore, the high resolution beam emitted from the tip of the antenna is narrow enough that multiple network areas can be built without interfering with each other.

These advantages will also enable Local 5G operators to fulfill the customers' requirements within a short period. In terms of processing materials, it can effectively reduce the cost of goods by at least 80%.

論文要旨

通信技術の急速な発展に伴い、信号処理に不可欠な部品であるアンテナやケーブルの需要は飛躍的に伸びている。独自にミリ波対応のローカル5G基地局を構築するためには特定帯域用の部品が必要でありミリ波対応アンテナやケーブルの需要が高まっている。

しかし、現在使用されているアンテナやケーブルなどの部品は、一定の加工費と加工時間が必要で、設計や実装に制約が生じる。さらに、特定の周波数や損失に対応したアンテナやケーブルについては、その特性上、より多くの時間と費用を要する。さらに、従来の部品で作られたインフラは一度部品を配置すると変更することができない、不可逆なものとなっている。これは、ネットワークエリアが少ない場合は許容範囲だが、ローカルネットワークの数が多く、アーキテクチャが複雑になると、ネットワーク同士の干渉につながってしまう。このため、よりコストと処理時間の少ない誘電体導波路を用いたミリ波アンテナを設計・製作し、分散型ローカルエリアネットワークを構築することを提案する。

本論文では、主に3種類の誘電体導波路アンテナを設計し、その設計過程、シミュレーションの詳細、そして製作物に対する評価について述べる。まず、関連する背景を紹介し、マクスウェルの電磁方程式と境界条件が誘電体導波路の特性とどのように結びついているかを紹介する。そして、アンテナの設計の基本理論を説明し、Sパラメータと半値幅が最適化されるようなパラメータでシミュレーションを行う。最後に誘電体導波路アンテナを製作し、実際の試験結果を観察し、スカラーネットワークアナライザやベクトルネットワークアナライザを用いて性能を実証する。

実際に製作したアンテナは、10dB以下の挿入損失と20度前後の半値幅を実現した。提案した実装方法は、簡単な原理と手順により、加工時間を1日以内に効率よく短縮することができる。さらに、アンテナ先端から放射される高分解能ビームは十分に細く、複数のネットワークエリアを相互に干渉させることなく構築することが可能となる。

以上により、5G事業者は短期間でネットワークエリアの仕様を満たすことができるようになる上、加工材料の面では、既存の材料を使うときに比べ80%以上のコスト削減が可能となる。

Acknowledgments

I want to express my deepest gratitude and appreciation to my advisor Professor Akihiro Nakao. Professor Akihiro Nakao has been supportive, friendly, and helpful throughout my master's program. His encouragement and understanding helped me overcome difficulties and created a space to develop my research ideas. I have always been fascinated by Professor Akihiro Nakao's insights in information science and his ability to identify and solve problems, and his example in time planning has enabled me to learn and apply it well in my research and daily life. Furthermore, his enthusiastic and open mentoring has sparked my interest in continuing more profound research in computer science, shaped my critical thinking, and challenged me to become a higher-level thinker.

Working with Professor Ping Du has been an enlightening and enriching experience. Whenever I needed advice, he was always quick and patient to help. Moreover, he was always polite and willing to share his experiences and views on persuasive research. I want to thank the various senior students and staff in the lab. They have helped and guided me in every way during the two years of my master's degree.

Most importantly, I would like to thank my family and friends for their continuous support and understanding with my pursuit of scientific research. Without their help, I would not have pursued my studies without worry. Finally, I would like to thank the official members of my examining committee for their efforts in reviewing my thesis and providing helpful suggestions.

Contents

1	Introduction	1
1.1	Background	1
1.2	Problem Statement	1
1.3	Thesis Statement	3
1.4	Related Work	4
1.5	Contributions	5
1.6	Organization	6
2	Mathematical Theory of Electromagnetism and Antennas	7
2.1	Mathematical analysis of waveguides	7
2.2	Horn Antennas	10
2.3	Radar	13
2.4	Antenna Gain	13
2.5	Antenna Impedance	13
2.5.1	Impedance in low frequencies	14
2.5.2	Impedance in high frequencies	15
2.6	The Friis Equation	16
2.7	Loss tangent	17
2.8	Skin effect	19
2.9	Snell's law	19
2.10	Total Reflection	20
2.11	Fresnel zone	21
2.12	Link budget	22
2.13	Scattering parameters (S-parameters)	23
2.13.1	Complex linear gain	24
2.13.2	Scalar linear gain	24
2.13.3	Scalar logarithmic gain	25
2.13.4	Insertion loss	25
2.14	Cutoff Frequency	25
2.15	Radiation Conditions	26
2.16	Variational Method	27
2.16.1	The Ritz Method	27

CONTENTS

2.16.2 A Simple example	28
2.17 Luneburg Lens	29
2.17.1 Uses in a microwave antenna	30
2.18 Summary	31
3 Qualitative Analysis of Dielectric Waveguide Antennas	32
3.1 Tools to Use	32
3.1.1 Vector network analyzers	32
3.1.2 MZ-mmCon1	33
3.1.3 MZ-mmAnt1	34
3.1.4 Shield Box	34
3.1.5 Adalm Pluto	34
3.1.6 Waveguide to Coax Adapter	36
3.1.7 Spectrum Analyzer	36
3.2 Communication Medium Used in Embedded Systems	36
3.2.1 UART	36
3.2.2 SPI	38
3.3 Qualitative Experiment with the Dielectric Waveguide	39
3.4 Summary	40
4 Quantitative Analysis of Dielectric Waveguide Antennas	41
4.0.1 Directivity Results	41
4.1 Summary	43
5 Dielectric Waveguide Antennas with Different Geometrical Tips	44
5.0.1 About the simulation conditions	44
5.0.2 About the models	44
5.0.3 S-parameter results from VNA based on simulation results	48
5.1 Summary	49
6 Conclusion	53
7 Future Work	54
Bibliography	55

List of Figures

1.1	Visibility between TX and RX is clear	3
1.2	Visibility between TX and RX is obscured by an obstacle	3
2.1	Model of metal waveguide	8
2.2	Geometry of metal waveguide	11
2.3	Cross section of waveguide, cut in the H-plane	11
2.4	Cross section of waveguide, cut in the E-plane	11
2.5	Model of horn antenna	12
2.6	Circuit model of antenna connected to voltage source	14
2.7	High frequency circuit model	15
2.8	Transmit (Tx) and Receive (Rx) Antennas separated by R	16
2.9	Comparison of Loss with Different Frequencies	18
2.10	Evanescence waves present in total internal reflection	21
2.11	Fresnel zone	22
2.12	Luneburg lens	30
3.1	MZ-mmcon1 in loopback mode	33
3.2	Adalm Pluto	33
3.3	FFT visualization on the software	34
3.4	mz-mmAnt1	35
3.5	Waveguide to Coax Adapter	35
3.6	Shield Box	35
3.7	VR-WH1 placed inside shield box	35
3.8	Conversion of the port on MS2762A	37
3.9	The mz-mmAnt1 hooked up to the MS2762A	37
3.10	UART with data bus	37
3.11	UART packet	38
3.12	SPI Communication	39
3.13	Video does not play (data is not received) when the waveguide is not pointed to the receiver	40
3.14	Video plays when the waveguide is pointed to the receiver	40
4.1	PTFE rod antenna with a diameter of 10 mm and length of 20 cm	41

LIST OF FIGURES

4.2	Placement of antenna in anechoic chamber	41
4.3	PTFE rod antenna in anechoic chamber	42
4.4	Horn antenna in anechoic chamber	42
4.5	Vertical Radiation Pattern	42
4.6	Horizontal Radiation Pattern	43
5.1	Solution Type for HFSS	45
5.2	Region Specification for HFSS	45
5.3	Waveport Models for HFSS	45
5.4	Solution Setup for HFSS	45
5.5	Integration Line for HFSS	46
5.6	Integration Line for HFSS for HFSS	46
5.7	HFSS simulation models	46
5.8	HFSS simulation models	47
5.9	Half power beamwidth of dome shaped antenna	48
5.10	S parameters of dome shaped antenna	49
5.11	Dielectric waveguide fabricated for the 28 GHz range	50
5.12	Comparison of S11 parameters with dielectric waveguide and no waveguide	51
5.13	Comparison of S21 parameters with dielectric waveguide and no waveguide	52

List of Tables

2.1	Comparisons of Preferred Gain	13
2.2	Table of all factors affecting the communication system	23

Chapter 1

Introduction

1.1 Background

The fifth generation (5G) mobile communication system is expected to provide new innovations to support the society with technical features including high speed, high capacity, low latency, and massive connectivity. 5G in a given area can support a far higher number of devices and larger data traffic, which has already seen in the last 10 years [1]. As a special feature of 5G, high frequency bands such as the millimeter wave bands are supported to achieve ultra-high speed wireless data communications of several gigabits per second using a frequency bandwidth of several-hundred megahertz [2]. This situation requires a reliable communication medium to ensure that the full capacity of mmWaves is utilized.

There are many types of components used in the 5G communication systems, such as SMA cables, K cables, horn antennas, and dielectric waveguides. Most of the components are designed to meet the requirements of higher operating frequency, guidance accuracy, and anti-interference capability by improving the specifications in the system. Under the above requirements, the weaknesses of SMA cables, K cables and horn antennas are apparent in the fact that they are heavy, rigid and expensive. Furthermore, the high resolution beam emitted from dielectric waveguides and horn antennas hinder developers and engineers from creating a local area network with wide coverage. However, dielectric waveguides have distinctive advantages, including their flexibility to be bent (although not in an angle too sharp [3]), cheaper costs, smaller weight, shorter delivery time, and its low loss characteristics in the millimeter wave band [4]. Therefore, new usecases of dielectric waveguides can be explored to provide a reliable and flexible infrastructure to users.

1.2 Problem Statement

Millimeter wave 5G technology can provide massive capacity and even lower latency than previous technologies such as 4G. This requires a 5G antenna with a low latency, low path

1.2. PROBLEM STATEMENT

loss, and a steady radiation pattern. However, millimeter waves also have problems and limitations that need to be addressed:

High cost of mmWave area construction Costly delivery of base station and horn antennas for area construction is high when building 5G communication systems. Overall size and internal structure of antennas differ according to their corresponding frequency bands. Therefore, when processing high-frequency antennas for small sizes, the corresponding processing accuracy is bound to increase. This leads to higher processing costs.

Irreversibility of mmWave area construction Equipment and devices for constructing a mmWave area are generally heavy, fixed and normally irreversible once construction has been completed.

Long delivery time

Customers need to make reservations, place orders in advance and wait long for manufacturers to produce and deliver. Moreover, it takes more time and expense for specific mmWave antennas because of their particular characteristics.

Performance degradation in environments with densely populated devices In an environment with densely populated devices, performance of the communication system deteriorates both in terms of speed and latency. Adding new wireless networks can mitigate this problem, but is not very effective for areas in similar frequency ranges. Multiple-input/multiple-out (MIMO) technology is an established wireless communications technique for sending and receiving multiple data signals simultaneously over the same radio channel. 5G New Radio introduces the concept of massive MIMO, which involves the MIMO technology on a larger scale for greater network coverage and capacity. However, this introduces new challenges, one of them being the cost of implementation and delivery. Device designers must understand the 3D beam patterns and ensure the beams can connect to the base station and deliver the desired performance, reliability, and user experience. This can result in higher design and implementation costs.

In addition to these general drawbacks, propagation losses in non-line-of-sight (NLOS) also need to be taken into account, as seen in Figure 1.2. mmWave communication is generally known to have high performance in line-of-sight (LOS) environments (Figure 1.1). However, as the received power on the device in a NLOS environment decreases, the communication area becomes much smaller than when utilizing lower frequency bands, and is one of the crucial issues in the millimeter wave bands. Technical solutions are provided by beamforming and beam steering techniques employing array antenna systems [5] [6] [7] [8] [9], which mitigate these issues and are actually implemented in some 5G base station equipment [?].

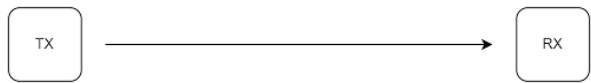


Fig. 1.1: Visibility between TX and RX is clear

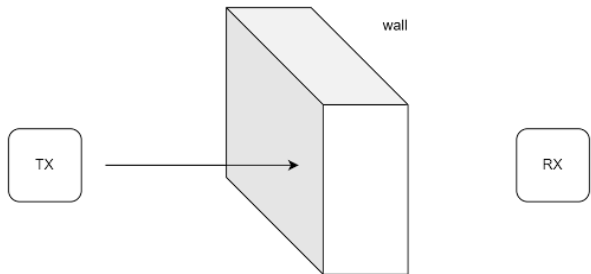


Fig. 1.2: Visibility between TX and RX is obscured by an obstacle

1.3 Thesis Statement

In order to efficiently solve the problems mentioned above, we propose to design a high resolution antenna using dielectric materials. We fabricate the antenna by processing a PTFE structure into a rod antenna. In this paper, we use the proposed processing methods to simulate, produce and test three different structures of dielectric antennas. The implemented antennas can achieve a resolution of 20 degrees half-power beamwidth and less than 10 dB of insertion loss. The test results show that the manufactured antennas can meet the functional requirements within a certain range. The proposed implementation method shows advantages in the following aspects.

Cost efficiency In response to the problem we identified regarding the high cost, the dielectric waveguide antennas implemented in this paper use PTFE to create the high resolution antenna. PTFE can vastly reduce the material cost and thus the antenna price.

Shorter lead time In terms of the problems of long processing time and long delivering time, this paper details the process from simulating the antenna to production; this presents a procedural process that can be followed strictly to design and produce an antenna that meets the conditions. The overall time required for implementing the antenna can be done within a few days, which can save much more time for both manufacturer and customer.

Flexibility of infrastructure Using the dielectric waveguides discussed in this paper, it is possible to exchange the components of the network communication

1.4. RELATED WORK

system without affecting the whole system. This allows users to customize the resolution and coverage of each network.

Improved fault isolation Under a monolithic network area structure, when engineers experience a failure in one element of the architecture, it will collapse all architecture components. With the type of distributed network area system discussed in our paper, if one service fails, it's much less likely that other parts of the application will fail because each network runs independently.

Scalability improvements Since each network area runs independently, it is easier to add, remove, update or scale each network, depending on the demand of traffic in the area. Designers and engineers can perform these tasks without disrupting any other network in the system. It is possible to create a network for environments where devices are densely populated, such as in a factories and farmlands

1.4 Related Work

Substrate integrated waveguides is a common low-cost mmWave technology that uses standard PCB techniques and allows easy integration with other circuits [10, 11, 12, 13, 14,]. The advantages of being low-cost, simple to manufacture, and easy end-to-end integration with other circuits enable acceleration of its development. Razavi et al. have designed mmWave planar antennas by employing the substrate integrated waveguide technology [15]. However, dielectric losses of the transmission line rise sharply as the operating frequency increases [16]. Although the substrate integrated waveguides show competitiveness in terms of manufacture and cost, the radiation efficiency is inevitably deteriorated, which limits its application in higher frequency band.

Studies on the groove gap waveguide slot array antenna are also increasing recently, as seen in [17]. Each plate, with small air gaps in between, does not need to have electrical contact with the neighboring plates. The electromagnetic (EM) wave leakage is suppressed by the semiperiodic array of metallic pins along with a metallic top plate [18, 19, 20, 21, 22,]. However, each plate of the mentioned antennas is complex and contains many protrusion structures based on thick metallic plates leading to expensive fabrication.

Hollow waveguide slot array antennas are also excellent candidates for high-frequency radiation systems due to low transmission loss and high power capacity [23] [24]. Numerous manufacturing techniques have been used to implement mmWave waveguide slot array antennas. Diffusion bonding of laminated plates and welding assembly technologies have been used to ensure robust contact without leakage [25] [26]. However, these manufacturing technologies are generally expensive and unsuitable for mass production.

For high-frequency radiation systems, Jin et al. have proposed a waveguide based on multilayer integrated vertical-EBG structure that can be manufactured with less cost [27]. A vertical-EBG structure is designed to eliminate the EM wave leakage in the air gap. A phase cancellation method is applied in spaces to narrow to set up EBG unit cells when

designing the slot array antenna structure. However, this still requires chemical etching techniques, which may be inconvenient in places with geographical restrictions.

The waveguides and antennas mentioned above all still have the similar limitations in their rigid structure and weight, which make them immobile. Furthermore, they still require high costs and long lead times for manufacturing, especially mass production, as all of them require some metallic and chemical processing.

Dielectric materials have been used as antennas for some time. In millimeter wave bands, Kawai et al. have proposed an approach that expands communication areas by using a flexible dielectric waveguide, which has low loss characteristics in the millimeter wave band range [28]. Fukuda et al. have proposed a leaky-wave antenna employing a bent dielectric waveguide for millimeter wave bands [29]. The study utilizes the characteristics that the dielectric waveguide radiates electromagnetic waves by inflection, and that the inflected part of the waveguide acts as an antenna. Since the inflected part can be formed anywhere along the length of the waveguide, it is possible to expand communication areas around the waveguide. Antenna gain values of 3 dB to 5 dB are achieved in both H-plane and V-plane, and a narrow beam was created in the V-plane.

1.5 Contributions

Compared to existing work and communication mediums, the designed dielectric antenna can achieve enhanced resolution with less loss and more flexibility. Moreover, the proposed methods show the advantages in the following aspects compared to the traditional manufacturing techniques.

Cost efficient The proposed method employs inexpensive PTFE material. The whole process also effectively reduces the cost of manufacturing antennas from scratch.

Shorter lead time The PTFE takes a few days at most for delivery and can be directly used without tuning, which is much shorter compared to existing horn antennas and patch antennas. This significantly reduces the lead time of the antenna.

Flexibility of infrastructure The PTFE rod antenna changes its resolution based on the geometrical shape of its attached tip. This allows users to dynamically change the coverage of the network area based on their purposes.

Improved fault isolation By utilizing the high resolution beam created by the rod antenna, the network areas all do not affect the quality of nearby networks and work independently of each other, which makes maintenance easier.

Scalability improvements Since all networks run independently of each other, it is easy to add and delete new network areas in the given environment.

1.6 Organization

This paper designs a high resolution PTFE rod antenna and details the design and implementation process.

The thesis chapters are organized as follows.

Chapter 1: First, We introduce the background of the communication system and dielectric waveguides. Then we elaborate the problem statement and thesis statement. At last, we describe the existing methods and their limitations and introduce the innovations and contributions of the paper.

Chapter 2: First, the theory of electromagnetic waves is discussed to understand basis of waveguides and antennas. Maxwell's equations and the laws derived from the equations are introduced in detail.

Chapter 3:

Chapter 4:

Chapter 5:

Chapter 6: Conclusion of this thesis

Chapter 7: Outlook of the future work

Chapter 2

Mathematical Theory of Electromagnetism and Antennas

2.1 Mathematical analysis of waveguides

Waveguides are devices for transporting electromagnetic energy from one region to another. There are a variety of waveguides, from hollow tubes made out of metal to sticks made of teflon. First we analyze waveguides that are hollow metal tubes (often rectangular or circular in cross section). These waveguides are capable of directing power precisely to where it is needed, can handle large amounts of power and function as a high-pass filter.

Here we examine metal waveguides with a rectangular cross section. In a source-free region, it is known that

$$\nabla D = 0 \quad (2.1)$$

where D is the electric flux density. If a vector quantity is divergenceless, then it can be expressed as the curl of another quantity. The solution for D and the corresponding electric field E can be written as:

$$D = -\nabla \times F \quad (2.2)$$

$$E = \frac{-1}{\epsilon} \nabla \times F \quad (2.3)$$

where ϵ is the permittivity of the medium where the wave propagates. Here for simplicity, it is assumed that E_z is zero. The following equations describing the electric and magnetic fields can be derived from Maxwell's equations.

$$E_x = -\frac{1}{\epsilon} \frac{\partial F_z}{\partial y} \quad (2.4)$$

2.1. MATHEMATICAL ANALYSIS OF WAVEGUIDES

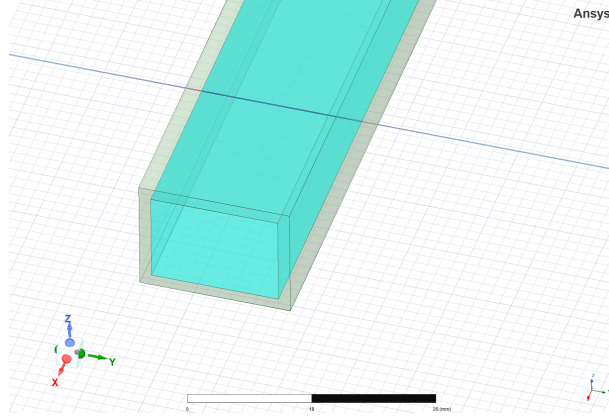


Fig. 2.1: Model of metal waveguide

$$E_y = \frac{1}{\epsilon} \frac{\partial F_z}{\partial x} \quad (2.5)$$

$$E_z = 0 \quad (2.6)$$

$$H_x = -j \frac{1}{\omega \mu \epsilon} \frac{\partial^2 F_z}{\partial x \partial z} \quad (2.7)$$

$$H_y = -j \frac{1}{\omega \mu \epsilon} \frac{\partial^2 F_z}{\partial y \partial z} \quad (2.8)$$

$$H_z = -j \frac{1}{\omega \mu \epsilon} \left(\frac{\partial^2}{\partial z^2} + k^2 \right) F_z \quad (2.9)$$

Here, k is the wave number. If the F_z , which is the z-axis component of the vector F , is found, then the electric and magnetic fields can be found. From Maxwell's equations, the vector potential F must satisfy the vector wave equation in a source-free region.

$$\left(\nabla^2 - \frac{1}{c^2} \frac{\partial^2}{\partial t^2} \right) \mathbf{F} = 0 \quad (2.10)$$

Assuming that there is only one frequency, the time dependence can be written as

$$e^{j\omega t} = e^{j2\pi f t} \quad (2.11)$$

Thus, the equation [2.10] can be rewritten as follows:

$$\nabla^2 F_z + k^2 F_z = 0 \quad (2.12)$$

The technique of separation of variables is used to solve this equation. It can be assumed that F_z can be separated into the product of 3 functions.

$$F_z(x, y, z) = X(x)Y(y)Z(z) \quad (2.13)$$

Therefore, when equation [2.13] is plugged into equation [2.12], the following equation is derived (the prime represents the derivative):

$$\frac{X''}{X} + \frac{Y''}{Y} + \frac{Z''}{Z} = -k^2 \quad (2.14)$$

For simplicity, the wavenumber k will be broken into components as below:

$$k^2 = k_x^2 + k_y^2 + k_z^2 \quad (2.15)$$

Using equation [2.15] and the fact that all variables are independent in equation [2.14], the following ordinary differential equations are derived:

$$\begin{cases} X'' + k_x^2 X = 0 \\ Y'' + k_y^2 Y = 0 \\ Z'' + k_z^2 Z = 0 \end{cases} \quad (2.16)$$

Solving the above equations, we get:

$$\begin{cases} X(x) = c_1 \cos(k_x x) + c_2 \sin(k_x x) \\ Y(y) = c_3 \cos(k_y y) + c_4 \sin(k_y y) \\ Z(z) = c_5 e^{jk_z z} + c_6 e^{-jk_z z} \end{cases} \quad (2.17)$$

The variable c_5 can be eliminated as 0, since waves analyzed here are propagating in the $+z$ direction. Plugging in the solutions above, F_z can be written as

$$F_z = [c_1 \cos(k_x x) + c_2 \sin(k_x x)][c_3 \cos(k_y y) + c_4 \sin(k_y y)]c_6 e^{-jk_z z} \quad (2.18)$$

Using the condition that tangential electric fields in perfect conductors must be zero, E_x must be zero when $y = 0$ and $y = b$. The same could be said for E_y , which is also zero when $x = 0$ and $x = a$. E_x can be calculated as:

$$\begin{aligned} E_x &= -\frac{1}{\epsilon} \frac{\partial F_z}{\partial y} \\ &= -\frac{c_6 k_y}{\epsilon} [c_1 \cos(k_x x) + c_2 \sin(k_x x)][-c_3 \sin(k_y y) + c_4 \cos(k_y y)]e^{-jk_z z} \end{aligned} \quad (2.19)$$

The boundary condition for E_x is given by:

$$E_x(x, y = 0, z) = 0 \quad (2.20)$$

This implies that c_4 must be equal to zero. As for the second boundary condition,

$$E_x(x, y = b, z) = 0 \quad (2.21)$$

2.2. HORN ANTENNAS

This means that $c_3 \sin(k_y b) = 0$, which means that the wavenumber k_y can be written as follows:

$$k_y = \frac{n\pi}{b} \quad (2.22)$$

n here is a natural number. This states that the only solutions for $Y(y)$ function must be sinusoids, and must have a wavenumber which consists an integer number of multiples of a half-wavelength. Similarly in the y-axis, the following can be derived:

$$k_x = \frac{m\pi}{a} \quad (2.23)$$

This statement implies that the only functions of x that satisfy the differential equation and the required boundary conditions must be an integer multiple of half-sinusoids within the waveguide. Combining these results, the solution for F_z can be written as

$$\begin{aligned} F_z &= A \cos(k_x x) \cos(k_y y) \exp(-jk_z z) \\ &= A \cos\left(\frac{m\pi x}{a}\right) \cos\left(\frac{n\pi y}{b}\right) \exp(-jk_z z) \end{aligned} \quad (2.24)$$

Only certain distributions will satisfy the required differential equations and the boundary conditions. These configurations are called modes. Since this solution assumed that E_z is zero, this mode is written as the TE_{mn} mode.

Due to Maxwell's Equations, the fields within the waveguide always have a specific "form" or "waveshape", which are known as modes. Assume the waveguide is oriented such that the energy is to be transmitted along the waveguide axis, the z-axis. The modes are classified as either TE ('transverse electric' - which indicates that the E-field is orthogonal to the axis of the waveguide, so that $E_z=0$) or TM ('transverse magnetic' - which indicates that the H-field is orthogonal to the axis of the waveguide, so $H_z = 0$). The modes are further classified as TE_{ij} , where the i and j indicate the number of wave oscillations for a particular field direction in the long direction (dimension a in Figure 2.2) and short direction (dimension b in Figure 2.2), respectively. Metal waveguides cannot support the TEM ('transverse electric and magnetic' - when E_z and H_z are zero) mode. There exists no solution to Maxwell's equations that also satisfy the required boundary conditions for this mode to occur.

2.2 Horn Antennas

Horn antennas are used in high frequency bands spanning from 300MHz to even as high as 100GHz. Horn antennas often have a directional radiation pattern with a high antenna gain, which can range up to 25 dB in some cases, with 10-20 dB being typical. Horn antennas have a wide impedance bandwidth, implying that the input impedance is slowly varying over a wide frequency range (which also implies low values for S11 or VSWR).

2.2. HORN ANTENNAS

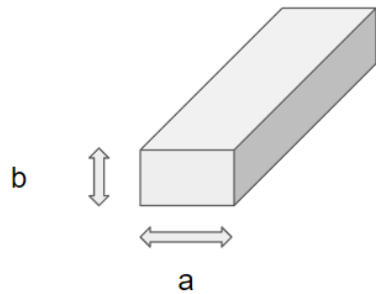


Fig. 2.2: Geometry of metal waveguide



Fig. 2.3: Cross section of waveguide, cut in the H-plane



Fig. 2.4: Cross section of waveguide, cut in the E-plane

2.2. HORN ANTENNAS

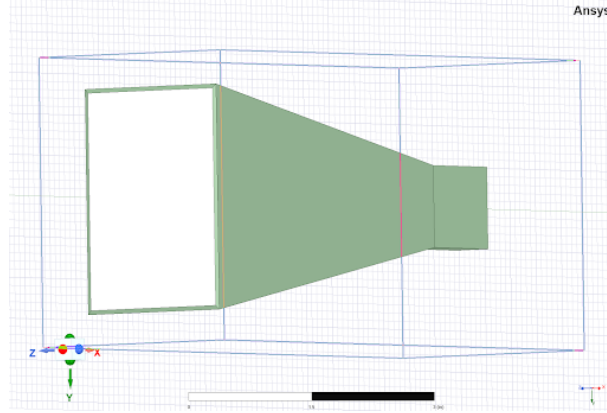


Fig. 2.5: Model of horn antenna

The bandwidth for practical horn antennas can be on the order of 20:1 (for instance, operating from 1 GHz-20 GHz), with a 10:1 bandwidth not being uncommon.

The E-field in the far-field becomes linearly polarized. The magnitude of the E-field can be written as:

$$|E| = \frac{k}{4\pi r} (1 + \cos(\theta)) \int_{-B/2}^{B/2} \int_{-A/2}^{A/2} E_A(x, y) e^{jk(x \sin \theta \cos \phi + y \sin \theta \sin \phi)} dx dy \quad (2.25)$$

This equation implies that the far-fields of the horn antenna is the Fourier Transform of the fields at the opening of the horn. Modeling the electric field as the magnetic surface current M_S , it can be written as:

$$M_S = E_a \times \hat{n} \quad (2.26)$$

\hat{n} is the unit vector perpendicular to the surface. The electric fields E and magnetic fields H in the far field can be written as:

$$E = \eta H \times \hat{r} \quad (2.27)$$

$$H = \hat{r} \times \frac{E}{\eta} \quad (2.28)$$

Here, η is the characteristic impedance of free space, which is about 377 Ohms. \hat{r} is the direction of propagation for the plane wave.

The waveguide feed acts as a high-pass filter, which blocks any energy below its cutoff frequency. The antenna gain is affected by the geometry of the horn antenna.

2.3 Radar

Radar works by transmitting an electromagnetic wave from an antenna. The wave then bounces off some object, and the returned energy is measured. The amount of energy returned is a function of the radar cross section of the object.

If we can estimate the fields radiated by an antenna, we can estimate the surface electric current induced on an object (such as an airplane).

2.4 Antenna Gain

The term antenna gain describes how much power is transmitted in the direction of peak radiation to that of an isotropic source. A transmitting antenna with a gain of 3 dB means that the power received far from the antenna will be 3 dB higher (twice as much) than what would be received from a lossless isotropic antenna with the same input power. Note that a lossless antenna would be an antenna with an antenna efficiency of 0 dB. Similarly, a receive antenna with a gain of 3 dB in a particular direction would receive 3 dB more power than a lossless isotropic antenna. Antenna Gain is sometimes discussed as a function of angle. In this case, we are essentially plotting the radiation pattern, where the units (or magnitude of the pattern) are measured in antenna gain. Often manufacturers of antennas (be they wifi antennas, gps antennas, or tv antennas) specify the antenna gain. For instance, manufacturers of wifi antennas may market the wifi antenna as a "high gain antenna", which is more expensive than a similar low gain antenna. Here we discuss how different devices have different gain, as the need for high/low gain differs depends on the situation.

Table 2.1: Comparisons of Preferred Gain

Example	Preferred Gain	Reason
TV antennas	High	Location of the broadcast antennas are known.
GPS	Low	Location of GPS satellites are unknown
Mobile Cellular Antennas	Low	Location of cell towers are unknown

2.5 Antenna Impedance

Antenna impedance relates the voltage to the current at the input to the antenna. This is an important parameter to look out for when conducting experiments.

For instance, when an antenna has an impedance of 50 ohms, this means that if a sinusoidal voltage is applied at the antenna terminals with an amplitude of 1 Volt, then the current will have an amplitude of $1/50 = 0.02$ Amps. Since the impedance is a real number, the voltage is in-phase with the current.

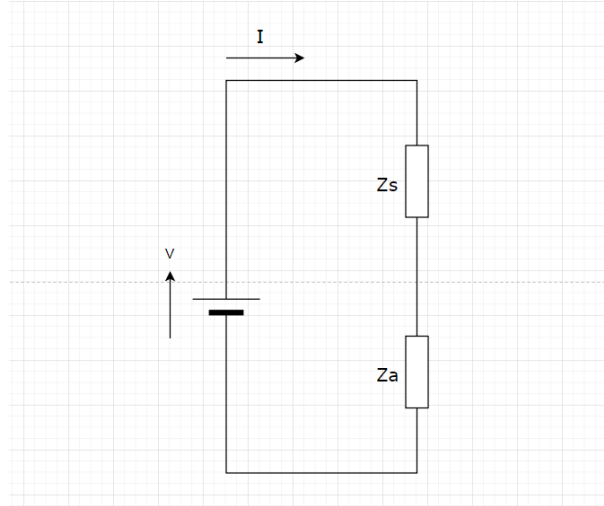


Fig. 2.6: Circuit model of antenna connected to voltage source

Alternatively, when the impedance is given by a complex number, the phase will need to be considered additionally to the amplitude. If impedance Z is written as $50 + j * 50$, where j is an imaginary number, then the impedance has a magnitude equal to:

$$\sqrt{50^2 + 50^2} = 70.71 \quad (2.29)$$

The phase can be calculated as:

$$\tan^{-1}\left(\frac{\text{Im}(Z)}{\text{Re}(Z)}\right) = \frac{\pi}{4} \quad (2.30)$$

The real part of the antenna impedance represents power that is either radiated away or absorbed within the antenna. The imaginary part of the impedance represents power that is stored in the near field of the antenna. This is non-radiated power. An antenna with a real input impedance (zero imaginary part) is said to be resonant.

2.5.1 Impedance in low frequencies

When we are dealing with low frequencies, the transmission line that connects the transmitter or receiver to the antenna is short relative to the wavelength.

Consider an antenna which is represented as an impedance given by Z_A , hooked up to a voltage source (of magnitude V) with source impedance given by Z_s . The equivalent circuit of this is shown in Figure 2.6.

Using the equation $P = IV$ from circuit theory, the power delivered to the antenna can be calculated as:

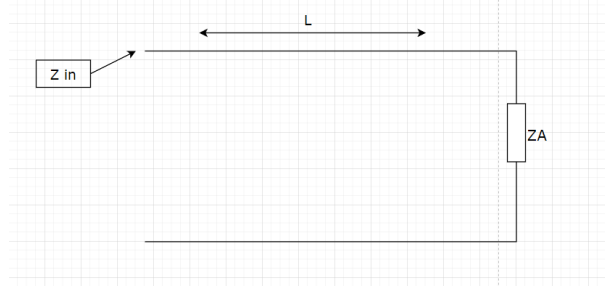


Fig. 2.7: High frequency circuit model

$$P_A = \frac{V^2 Z_A}{(Z_A + Z_S)^2} \quad (2.31)$$

If Z_A is much smaller in magnitude than Z_S , then no power will be delivered to the antenna and it won't transmit or receive energy. The same can be said when Z_A is much larger in magnitude than Z_S . The ideal value for antenna impedance when maximum power is transferred is given as:

$$Z_A = Z_S^* \quad (2.32)$$

where Z_S^* is the complex conjugate of Z_S . For example, if $Z_S = 30 + 30j$, then $Z_A = 30 - 30j$ is the ideal impedance for maximum power transfer.

2.5.2 Impedance in high frequencies

In low-frequency circuit theory, the wires that connect things don't matter. Once the wires become a significant fraction of a wavelength, the situation changes. For instance, a short circuit has an impedance of zero ohms. However, if the impedance is measured at the end of a quarter wavelength transmission line, the impedance appears to be infinite, even though there is a direct current conduction path.

In general, the transmission line will transform the impedance of an antenna, making it very difficult to deliver power, unless the antenna is matched to the transmission line. Consider the situation shown in Figure 2.7. The impedance is to be measured at the end of a transmission line (with characteristic impedance Z_0) and Length L . The end of the transmission line is hooked to an antenna with impedance Z_A .

Input impedance Z_{in} is given by:

$$Z_{in} = Z_0 \frac{Z_A + jZ_0 \tan(\frac{2\pi f}{c})L}{Z_0 + jZ_A \tan(\frac{2\pi f}{c})L} \quad (2.33)$$

If the antenna is matched to the transmission line ($Z_A = Z_0$), then the input impedance does not depend on the length of the transmission line.



Fig. 2.8: Transmit (Tx) and Receive (Rx) Antennas separated by R.

If the antenna is not matched, the input impedance will vary widely with the length of the transmission line. And if the input impedance isn't well matched to the source impedance, not very much power will be delivered to the antenna. This power ends up being reflected back to the generator, which can be a problem in itself (especially if high power is transmitted). This loss of power is known as impedance mismatch. Hence, having a tuned impedance for an antenna is extremely important.

2.6 The Friis Equation

One of the most fundamental equations in antenna theory is the Friis Transmission Equation. The Friis Transmission Equation is used to calculate the power received from one antenna (with gain G_1), when transmitted from another antenna (with gain G_2), separated by a distance R , and operating at frequency f or wavelength λ . The two antennas are considered to be in free space.

Assume that P_T watts of total power are delivered to the transmit antenna and that the transmit antenna is omnidirectional, lossless, and that the receive antenna is in the far field of the transmit antenna. Then the power density p (in Watts per square meter) from the transmit antenna is given by:

$$p = \frac{P_T}{4\pi R^2} \quad (2.34)$$

If the transmit antenna has an antenna gain in the direction of the receive antenna given by G_T , then the power density can be written as:

$$p = \frac{P_T}{4\pi R^2} G_T \quad (2.35)$$

The gain term factors in the directionality and losses of a real antenna. Assume now

2.7. LOSS TANGENT

that the receive antenna has an effective aperture given by $A_E R$. Then the power received by this antenna P_R is given by:

$$p = \frac{P_T}{4\pi R^2} G_T A_E R \quad (2.36)$$

Since the effective aperture for any antenna can also be expressed as:

$$A_e = \frac{\lambda^2}{4\pi} G \quad (2.37)$$

Plugging in this result, the received power can be rewritten as:

$$p = \frac{P_T G_T G_R \lambda^2}{(4\pi R)^2} \quad (2.38)$$

Equation 2.38 is the Friis Transmission Formula, and relates the free space path loss, antenna gains and wavelength to the received and transmit powers.

When we plug in the wave equation $c = f\lambda$, where c is the speed of light, f is the frequency, and λ is the wavelength, we get:

$$P_R = \frac{P_T G_T G_R c^2}{(4\pi R f)^2} \quad (2.39)$$

Equation 2.39 shows that more power is lost at higher frequencies. This means that for antennas with specified gains, the energy transfer will be highest at lower frequencies. The difference between the power received and the power transmitted is known as path loss.

Using 2.38, loss L (in decibels) in free space can be rewritten as follows:

$$L = \left(\frac{4\pi d}{\lambda} \right)^2 \quad (2.40)$$

At 28GHz, which has the wave length of 1 cm, the loss at the distance of 0.25 cm can be computed as -49.3 decibels. At 800MHz (wave length of 37.5 cm), the same loss of -49.3 decibels can be seen at the distance of 10 meters. The comparison of these two frequencies is shown in Figure 2.9.

2.7 Loss tangent

In a dielectric material, dielectric loss quantifies the inherent dissipation of electromagnetic energy, and can be parametrized in terms of the loss tangent. The basic equation for electromagnetic waves when there is loss in the medium is as follows

$$\text{rot}\left(\frac{1}{\mu(\mathbf{r})}\text{rot}\mathbf{E}\right) = -\mu_0\text{rot}\left(\frac{\partial H}{\partial t}\right) \quad (2.41)$$

2.7. LOSS TANGENT

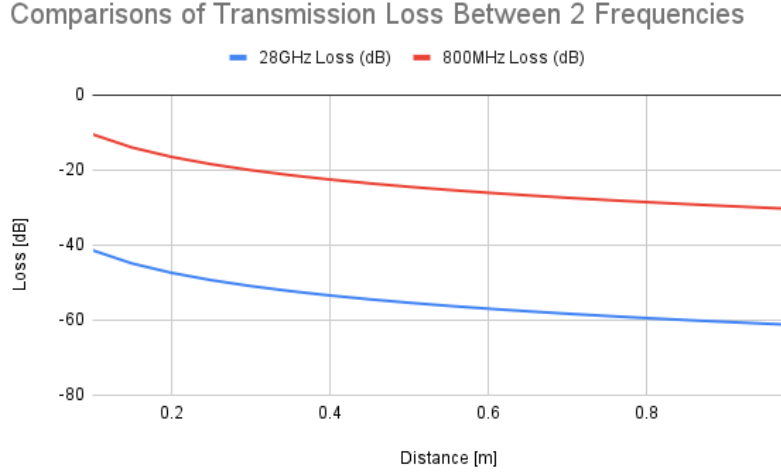


Fig. 2.9: Comparison of Loss with Different Frequencies

$$\text{rot}\left(\frac{\partial \mathbf{H}}{\partial t}\right) = \epsilon(\mathbf{r})\epsilon_0 \frac{\partial^2 \mathbf{E}}{\partial t^2} + \frac{\partial \mathbf{J}}{\partial t} \quad (2.42)$$

We consider the characteristic value when there is loss in the medium. When we consider the incidence of the time-varying factor $\exp(j\omega t)$, Maxwell's Equation can be written as follows.

$$\text{rot} \mathbf{H} = \epsilon\epsilon_0 \frac{\partial \mathbf{E}}{\partial t} + \sigma \mathbf{E} = (j\omega\epsilon\epsilon_0 + \sigma) \mathbf{E} \quad (2.43)$$

In this case, the right-hand side of Equation 2.43 is considered to arise from the flux density \mathbf{D} .

$$\mathbf{D} = C\epsilon\epsilon_0 \mathbf{E}(\mathbf{r}) \exp(j\omega t) \quad (2.44)$$

We derive the constant $C = 1 - j\sigma/\omega\epsilon\epsilon_0$ from the equation above. Thus the electric flux density can be written as

$$\mathbf{D} = \dot{\epsilon}\epsilon_0 \mathbf{E} = \epsilon\epsilon_0(1 - j\tan\delta) \mathbf{E} \quad (2.45)$$

$$\dot{\epsilon} = \epsilon(1 - j\tan\delta) \quad (2.46)$$

$$\tan\delta = \frac{\sigma}{\omega\epsilon\epsilon_0} \quad (2.47)$$

The parameter in Eq. 2.47 is known as the loss tangent. At high frequencies, the contribution of the real part of ϵ becomes larger, while at low frequencies, the contribution of the imaginary part becomes larger. In other words, it can be said that when an AC electric field is applied to a dielectric, a part of its energy is the ratio that becomes heat.

2.8 Skin effect

Skin effect is the tendency of an alternating current to flow mostly near the outer surface of an electrical conductor, such as copper plates. In many of the experiments in this study, millimeter waves are blocked by copper plates. The conductivity of the conductor σ increases, and the amplitude damping constant α and the phase constant β can be estimated as below.

$$\alpha \approx \beta \approx \sqrt{\frac{\omega \mu \mu_0 \sigma}{2}} \quad (2.48)$$

This means that the attenuation of electromagnetic waves increases with increasing conductivity of σ and the electromagnetic wave attenuates exponentially. The depth δ at which the amplitude of the electromagnetic wave at the surface is $1/e$ is called the skin depth, which can be expressed as below.

$$\delta = \frac{1}{\alpha} = \sqrt{\frac{2}{\omega \mu \mu_0 \sigma}} \quad (2.49)$$

This indicates that the skin depth becomes shallower as the frequency of the electromagnetic wave increases and the conductivity increases. In this case, the current flows only near the surface of the copper plate, which is called the skin effect. The fact that current flows means that resistance exists, and the skin resistance is written as follows.

$$Re\{Z_W\} = \sqrt{\frac{\omega \mu \mu_0}{2}} = \frac{1}{\delta \sigma} \quad (2.50)$$

Therefore copper plates can be used to effectively block millimeter waves.

2.9 Snell's law

At the boundary surfaces of different media, reflection and refraction of electromagnetic waves occur. This is described by Snell's law. This law can be derived using Maxwell's equations and boundary conditions.

The boundary plane of the medium is the x-y plane, and the medium is uniform in the y direction within each region. The relative permittivity and relative permeability are ϵ_1 and μ_1 for the first medium, and ϵ_2 and μ_2 for the second medium. Let the complex permittivity in the presence of loss be i for each medium, so take values of 1 and 2, respectively.

$$\epsilon_i = \epsilon(1 - j \frac{\sigma_i}{\omega \epsilon_i \epsilon_0}) \quad (2.51)$$

Here σ is the conductivity, ω is the angular frequency of the electromagnetic wave, ϵ is the dielectric constant when there is no loss, and ϵ_0 is the dielectric constant of vacuum.

2.10. TOTAL REFLECTION

The specific permeability μ is assumed to be a real number this time. Here the magnitude of the wavenumber of each medium is as follows as k . c is the speed of light in vacuum.

$$k_i = \frac{\omega\sqrt{\epsilon_i\mu_i}}{c} \quad (2.52)$$

Here we derive Snell's law using the TE wave as an example. For TE waves, the oscillation direction of the electric field is perpendicular to the surface, and there is no electric field component in the direction of propagation. Since the direction perpendicular to the surface is the y -axis, its electric field is E_y^i and can be written as follows:

$$E_y^i = A_{iS} \exp[j(\omega t - \mathbf{k}_i \cdot \mathbf{r})] \quad (2.53)$$

A_{iS} is the electric field amplitude, \mathbf{k}_i is the wavenumber vector in the medium, and \mathbf{r} is the position vector to an arbitrary point on the wavefront. The subscript i has three states, where incident, transmitted, and reflected are denoted by i, t, and r, respectively.

2.10 Total Reflection

When an electromagnetic wave is incident on a sparse medium from a dense medium, the refraction angle reaches 90 degrees before the incident angle as the incident angle is gradually increased. This phenomenon in which the incident electromagnetic wave returns to the incident side after being reflected at the boundary surface without being transmitted is called total reflection.

The transmitted field components of the TE wave at total reflection can be written as follows.

$$E_y^t = \exp[-j(\sqrt{\epsilon_1\mu_1} k_0 \sin \theta_t) x] \exp\left(-\frac{z}{z_g}\right) \quad (2.54)$$

$$z_g = \frac{c}{\omega\sqrt{\epsilon_1\mu_1 \sin^2 \theta - \epsilon_2\mu_2}} \quad (2.55)$$

z_g represents the depth of penetration of the electric field into the second medium, indicating that the electromagnetic wave is seeping slightly into the boundary surface. Even during total reflection, electromagnetic waves also slightly penetrate to the other side of the boundary. This component is called the evanescent wave. Along with the penetration of the electromagnetic field, the reflection point is also shifted. This shift is called the Guschenchen shift. This is important when using dielectric waveguides and optical fibers.

Electromagnetic waves do seep out slightly to the other side of the boundary plane, but it is important to note that the energy does not seep out. It is important to note that energy does not seep out. The sum of the amplitude reflection coefficients all add up to 1, and all energy is also reflected.



Fig. 2.10: Evanescence waves present in total internal reflection

2.11 Fresnel zone

A Fresnel zone is one of a series of confocal prolate ellipsoidal regions of space between and around a transmitter and a receiver. The primary wave will travel in a relative straight line from the transmitter to the receiver. The concept of Fresnel zone clearance may be used to analyze interference by obstacles near the path of a radio beam. The first zone must be kept largely free from obstructions to avoid interfering with the radio reception. For establishing Fresnel zones, first determine the RF line of sight (RF LoS), which in simple terms is a straight line between the transmitting and receiving antennas. Now the zone surrounding the RF LoS is said to be the Fresnel zone. The cross sectional radius of each Fresnel zone is the longest at the midpoint of the RF LoS, shrinking to a point at each vertex, behind the antennas.

To formulate the Fresnel zone, we consider an arbitrary point P in the LoS, at a distance d_1 and d_2 with respect to each of the two antennas. To obtain the radius r_n of zone n , note that the volume of the zone is delimited by all points for which the difference in distances, between the direct wave $D = d_1 + d_2$ and the reflected wave is the constant of $n\frac{\lambda}{2}$. This effectively defines an ellipsoid with the major axis along \overline{AB} and foci (points A and B) at the antennas.

$$\overline{AP} + \overline{PB} - D = n\frac{\lambda}{2} \quad (2.56)$$

Rewriting the expression using d_1 , d_2 , and r_n , the equation can be given as:

$$d_1 \left(\sqrt{1 + r_n^2/d_1^2} \right) + d_2 \left(\sqrt{1 + r_n^2/d_2^2} - 1 \right) = n\frac{\lambda}{2} \quad (2.57)$$

By applying binomial approximation for the square root, r_n can be solved as:

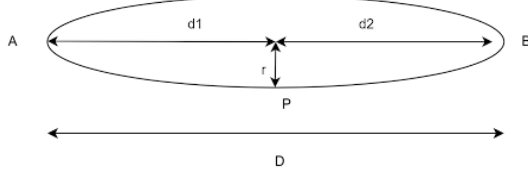


Fig. 2.11: Fresnel zone

$$r_n \approx \sqrt{n \frac{d_1 d_2}{D} \lambda} \quad (2.58)$$

where $d_1, d_2 \gg n\lambda$.

For a satellite-to-Earth link, it further simplifies to [30]:

$$r_n \approx \sqrt{nd_1\lambda}, \quad d_1 \gg n\lambda, \quad d_2 \approx D \quad (2.59)$$

2.12 Link budget

A link budget is an accounting of all of the power gains and losses that a communication signal experiences in a telecommunication system; from a transmitter, through a communication medium such as radio waves, cable, waveguide, or optical fiber, to the receiver. Link budget is controlled by three factors, which are communication distance, transmitted power, and antenna gain.

To calculate the link budget, we first need to calculate the EIRP (Equivalent Isotropically Radiated Power)[W], which is the sum of the output power of the transmitter, antenna gain, and cable loss, which can be written as follows:

$$EIRP = TP + Gain - Loss \quad (2.60)$$

EIRP and TP are short for received power and transmitted power, respectively. While EIRP and TP are in units of decibels-milliwatts, gain and loss are in units of decibels. TP is further determined by the cable loss and the transmitted power of the device itself. Here we omit some variables such as miscellaneous losses, which include polarization mismatch and fading margin.

For example, when the input power of the transmitter and the gain is -11 dBm and 5 dBi, respectively, the EIRP is -6 dBm. If the gain on the receiver antenna is 5dBi and the path loss is 49.3 dB, the received power on the receiver antenna can be calculated as:

$$P_r = EIRP - L_a + G_r = -50.3dBm \quad (2.61)$$

The table below summarizes the situation discussed above:

Table 2.2: Table of all factors affecting the communication system

Factors	Values	Unit
Tx Power	-10	dBm
Tx Cable Loss	-1	dB
Tx ANT Gain	5	dBi
EIRP	-6	dBm
Distance	0.25	m
Air loss	-49.3	dBi
Rx ANT Gain	5	dBi
Rx Cable Loss	-1	dB
Rx Input	-51.3	dBm

This indicates again the limitations of the millimeter wave in an open space. Millimeter waves with frequency of 28GHz have a loss of -49.3 dB just within 0.25 meters of communication distance.

2.13 Scattering parameters (S-parameters)

Scattering parameters or S-parameters (the elements of a scattering matrix or S-matrix) describe the electrical behavior of linear electrical networks when undergoing various steady state stimuli by electrical signals. S-parameters do not use open or short circuit conditions to characterize a linear electrical network; instead, matched loads are used. These terminations are much easier to use at high signal frequencies than open-circuit and short-circuit terminations.

For a generic multi-port network, the ports are numbered from 1 to N , where N is the total number of ports. For port i , the associated S-parameter definition is in terms of incident and reflected 'power waves', a_i and b_i , respectively. Kurokawa [31] defines the incident power wave for each port as

$$a_i = \frac{1}{2}k_i(V_i + Z_i I_i) \quad (2.62)$$

and the reflected wave for each port is defined as

$$b_i = \frac{1}{2}k_i(V_i - Z_i^* I_i) \quad (2.63)$$

Here Z_i is the impedance for port i , Z_i^* is the complex conjugate of Z_i , V_i and I_i are respectively the complex amplitudes of the voltage and current at port i , and

$$k_i = \left(\sqrt{|Re(Z_i)|} \right)^{-1} \quad (2.64)$$

2.13. SCATTERING PARAMETERS (S-PARAMETERS)

The relation between the vectors \mathbf{a} and \mathbf{b} , whose i -th components are the power waves a_i and b_i respectively, can be expressed using the S-parameter matrix S :

$$\mathbf{b} = \mathbf{Sa} \quad (2.65)$$

When using explicit components, the equation above can be rewritten to:

$$\begin{pmatrix} S_{11} & \dots & S_{1n} \\ \vdots & \ddots & \vdots \\ S_{n1} & \dots & S_{nn} \end{pmatrix} \quad (2.66)$$

Next, we consider two-port S-parameters. In this case the relationship between the reflected, incident power waves and the S-parameter matrix is given by:

$$\begin{pmatrix} b_1 \\ b_2 \end{pmatrix} = \begin{pmatrix} S_{11} & S_{12} \\ S_{21} & S_{22} \end{pmatrix} \begin{pmatrix} a_1 \\ a_2 \end{pmatrix} \quad (2.67)$$

Each value of the S-parameter matrix has the following generic descriptions:

- S_{11} is the input port voltage reflection coefficient
- S_{12} is the reverse voltage gain
- S_{21} is the forward voltage gain
- S_{22} is the output port voltage reflection coefficient.

2.13.1 Complex linear gain

The complex linear gain G is given by

$$G = S_{21} = \frac{b_2}{a_1} \quad (2.68)$$

That is the linear ratio of the output reflected power wave divided by the input incident power wave, all values expressed as complex quantities. For lossy networks it is sub-unitary, for active networks $|G| > 1$. It will be equal with the voltage gain only when the device has equal input and output impedances.

2.13.2 Scalar linear gain

The scalar linear gain (or linear gain magnitude) is given by

$$|G| = |S_{21}| \quad (2.69)$$

This represents the gain magnitude (absolute value), the ratio of the output power-wave to the input power-wave, and it equals the square-root of the power gain. This is a real-value (or scalar) quantity, the phase information being dropped.

2.13.3 Scalar logarithmic gain

The scalar logarithmic (decibel or dB) expression for gain (g) is:

$$g = 20 \log_{10} |S_{21}| \quad (2.70)$$

This is more commonly used than scalar linear gain and a positive quantity is normally understood as simply a "gain", while a negative quantity is a "negative gain" (a "loss"), equivalent to its magnitude in dB. For example, at 100 MHz, a 10 m length of cable may have a gain of -1 dB, equal to a loss of 1 dB.

2.13.4 Insertion loss

In case the two measurement ports use the same reference impedance, the insertion loss (IL) is the reciprocal of the magnitude of the transmission coefficient — S_{21} — expressed in decibels. It is thus given by

$$IL = -20 \log_{10} |S_{21}| \quad (2.71)$$

It is the extra loss produced by the introduction of the device under test (DUT) between the 2 reference planes of the measurement. The extra loss may be due to intrinsic loss in the DUT and/or mismatch. In case of extra loss the insertion loss is defined to be positive. The negative of insertion loss expressed in decibels is defined as insertion gain and is equal to the scalar logarithmic gain.

2.14 Cutoff Frequency

A cutoff frequency, corner frequency, or break frequency is a boundary in a system's frequency response at which energy flowing through the system begins to be reduced rather than passing through. This means that the signals with a frequency above the cut-off frequency will travel through a waveguide and signals below this frequency will be attenuated.

Using the fact that the components of the wavenumber must satisfy the relationship:

$$k_x^2 + k_y^2 + k_z^2 = \omega^2 \mu \epsilon = \left(\frac{2\pi f}{c} \right)^2 \quad (2.72)$$

Assuming the situations are the same as in the equations 2.22 and 2.23, by plugging them in we get:

$$\left(\frac{m\pi}{a} \right)^2 + \left(\frac{n\pi}{b} \right)^2 + k_z^2 = k^2 = \left(\frac{2\pi f}{c} \right)^2 \quad (2.73)$$

$k_z^2 > 0$ is the necessary condition for propagation to occur. If this is true, then k_z is a real number, so that the field components will contain complex exponentials,

which represent propagating waves. Otherwise when $k_z^2 < 0$, k_z will be an imaginary number, in which case the complex exponential becomes a decaying real exponential. In this case, the fields will not propagate but instead quickly die out within the waveguide. Electromagnetic fields that die off instead of propagate are referred to as evanescent waves.

By setting $k_z = 0$, the lowest frequency in which propagation occurs can be found. This is the transition between the cutoff region (evanescent) and the propagation region. Equation 2.73 can be rewritten as:

$$\left(\frac{m\pi}{a}\right)^2 + \left(\frac{n\pi}{b}\right)^2 = \left(\frac{2\pi f}{c}\right)^2 \quad (2.74)$$

The lowest value the left hand side of the equation can take occurs when $m = 1$ and $n = 0$. This gives the cutoff frequency for this waveguide:

$$f_c = \frac{c}{2a} \quad (2.75)$$

Generally, cutoff frequency f_c in a rectangular waveguide can be calculated as follows, where a is the wall length, and μ and ϵ are the permeability and permittivity of the material that fill the waveguide, respectively.

$$f_c = \frac{1}{2a\sqrt{\mu\epsilon}} \quad (2.76)$$

In a circular waveguide with radius of a , f_c could be written as

$$f_c = \frac{1.8412}{2\pi a\sqrt{\mu\epsilon}} \quad (2.77)$$

2.15 Radiation Conditions

When the outer boundary of a domain recedes to infinity, the domain is called unbounded or open. A condition must be specified at this outer boundary to obtain a unique solution for this problem. Such a condition is referred to as a radiation condition.

Assuming that all sources and objects are immersed in free space and located within a finite distance from the origin of a coordinate system, the electric and magnetic fields are required to satisfy:

$$\lim_{r \rightarrow \infty} \left[\nabla \times \begin{pmatrix} \mathbf{E} \\ \mathbf{H} \end{pmatrix} + jk_0 \hat{r} \times \begin{pmatrix} \mathbf{E} \\ \mathbf{H} \end{pmatrix} \right] = 0 \quad (2.78)$$

where $r = \sqrt{x^2 + y^2 + z^2}$. This is referred to as the Sommerfeld radiation condition for general three-dimensional fields, and is exactly valid at infinity. In numerical analysis, it is often desirable to reduce the size of a computational domain by using a finite boundary to truncate the infinite domain. When applied at such a finite boundary, 2.78 can be regarded as the lowest-order radiation condition with limited accuracy. Better accuracy can be achieved by developing higher-order conditions.

2.16 Variational Method

A typical boundary-value problem can be defined by a governing differential equation in a domain Ω , and the boundary conditions on the boundary Γ that encloses the domain.

$$L\phi = f \quad (2.79)$$

Here L is a differential operator, f is the excitation function, and ϕ is the unknown quantity. Poisson equation is an example of a governing differential equation in electromagnetics and Dirichlet condition is an example of a boundary condition.

2.16.1 The Ritz Method

The operator L is self-adjoint when it satisfies the following condition:

$$\langle L\phi, \psi \rangle = \langle \phi, L\psi \rangle \quad (2.80)$$

An example of a self-adjoint operator is $i \frac{d}{dx}$. (A simple instance of this can be calculated by using the operator on $\phi = e^{ix}$. Check the following $[L\phi]\phi^* = \phi[L^*\phi^*]$ is satisfied) To obtain the solution, we must add another condition that the operator L is positive definite, that is:

$$\langle L\phi, \phi \rangle = \begin{cases} > 0 & \phi \neq 0 \\ = 0 & \phi = 0 \end{cases} \quad (2.81)$$

And the solution to Equation 2.80 can be obtained by minimizing the functional

$$F(\tilde{\phi}) = \frac{1}{2} \langle L\tilde{\phi}, \tilde{\phi} \rangle - \langle \tilde{\phi}, f \rangle - \langle f, \tilde{\phi} \rangle \quad (2.82)$$

Here $\tilde{\phi}$ represents a trial function. To prove this variational principle, we first need to show the differential equation is the necessary consequence when the functional F is stationary ($\delta F = 0$). We also must prove that the stationary point is at the minimum of the functional F , which is equivalent to proving that $\delta(\delta F) > 0$. Taking the variation again,

$$\delta F = \frac{1}{2} \langle L\delta\phi, \phi \rangle + \frac{1}{2} \langle L\phi, \delta\phi \rangle - \frac{1}{2} \langle \delta\phi, f \rangle - \frac{1}{2} \langle f, \delta\phi \rangle \quad (2.83)$$

and using the condition is that L is self-adjoint,

$$\frac{1}{2} \langle L\delta\phi, \phi \rangle = \frac{1}{2} \langle L\phi, \delta\phi \rangle \quad (2.84)$$

allows us to simplify the equation as follows:

$$\delta F = \frac{1}{2} \langle \delta\phi, L\phi - f \rangle - \frac{1}{2} \langle L\phi - f, \delta\phi \rangle \quad (2.85)$$

The definition of the inner product lets us have

$$\delta F = \frac{1}{2} \langle \delta\phi, L\phi - f \rangle - \frac{1}{2} \langle \delta\phi, L\phi - f \rangle^* = \text{Re} \langle \delta\phi, L\phi - f \rangle \quad (2.86)$$

Here Re denotes the real part of the equation it encloses. Imposing the stationary requirement $\delta F = 0$, we obtain

$$\text{Re} \langle \delta\phi, L\phi - f \rangle = \text{Re} \left\langle \int_{\Omega} \delta\phi (L\phi - f)^* d\Omega \right\rangle = 0 \quad (2.87)$$

$\delta\phi = 0$ can be ignored since it is an arbitrary variation, and from $L\phi - f = 0$, the first point is proved.

The second point can be considered by taking the first variation of δF once more. This results in:

$$\delta(\delta F) = \delta F(\phi + \delta\phi) - \delta F(\phi) = \text{Re} \langle \delta\phi, L\delta\phi \rangle \quad (2.88)$$

For a nontrivial (non-zero) $\delta\phi$, using the positive definite condition, we can conclude that $\delta(\delta F) > 0$. Rephrasing this, when $L > 0$ and $\delta\phi > 0$, the result of Equation 2.88 is greater than 0. Therefore the stationary point is indeed at the minimum of F .

2.16.2 A Simple example

Here we look at a simple boundary-value problem and solve it using the Ritz methods [32]. The problem is about the determination of the static potential ϕ between two infinite parallel plates. One plate is located at $x = 0$ with $\phi = 0$ and the other at $x = 1$ with $\phi = 1$. The space between is filled with a medium having a constant permittivity of ϵ F/m and a varying electric charge density of $\rho(x) = -(x + 1)\epsilon$ C/m³.

The Poisson equation can be applied to this problem as follows (we do not take off the minus at the both sides of the equation for simplicity):

$$-\frac{d^2\phi}{dx^2}\epsilon = -(x + 1)\epsilon \quad (2.89)$$

The boundary conditions are given as:

$$\phi|_{x=0} = 0 \quad (2.90)$$

$$\phi|_{x=1} = 1 \quad (2.91)$$

This is simply a second-order differential equation, and can be solved easily by integrating the equation twice. Here we assume we do not know the exact solution and use the Ritz and Galerkin methods to find it. Here we introduce the Ritz method.

Solution via the Ritz Method

In the Ritz method, a functional is defined where the minimum of the functional corresponds to the differential equation under the given boundary conditions. From eq. 2.80, the differential operator L is $-\frac{d^2}{dx^2}$ (which is a self-adjoint operator and satisfies the conditions to be used for the Ritz method), and $-(x + 1)$ is the forcing function. Plugging them into the equation 2.79, we get:

$$F(\tilde{\phi}) = \frac{1}{2} \int_0^1 \left(-\frac{d^2}{dx^2}\phi\right)\phi^* dx + \frac{1}{2} \int_0^1 \tilde{\phi}(x + 1)dx + \frac{1}{2} \int_0^1 (x + 1)\tilde{\phi}^* dx \quad (2.92)$$

Since the problem here does not contain imaginary numbers, we can say $\tilde{\phi} = \tilde{\phi}^*$. Also, since $i\frac{d}{dx}$ is also a self adjoint operator,

$$\left(-\frac{d^2}{dx^2}\tilde{\phi}\right)\tilde{\phi}^* = (i\frac{d}{dx}\tilde{\phi})(-i\frac{d}{dx}\tilde{\phi}^*) = (i\frac{d}{dx}\tilde{\phi})(i\frac{d}{dx}\tilde{\phi})^* = |(\frac{d}{dx}\tilde{\phi})|^2 \quad (2.93)$$

Therefore the functional equation can be simplified as:

$$F(\tilde{\phi}) = \frac{1}{2} \int_0^1 \left(\frac{d}{dx}\tilde{\phi}\right)^2 dx + \int_0^1 \tilde{\phi}(x + 1)dx \quad (2.94)$$

Here we use polynomials as one of the candidate trial functions:

$$\tilde{\phi}(x) = c_1 + c_2x + c_3x^2 + c_4x^3 \quad (2.95)$$

From the boundary conditions, the conditions $c_1 = 0$, $c_2 = 1 - c_3 - c_4$ are obtained. This reduces the current function to

$$\tilde{\phi}(x) = x + c_3(x^2 - x) + c_4(x^3 - x) \quad (2.96)$$

Substituting the above equation to 2.94, the following derivatives are obtained:

$$\frac{\partial F}{\partial c_3} = \frac{1}{3}c_3 + \frac{1}{2}c_4 - \frac{1}{4} \quad (2.97)$$

$$\frac{\partial F}{\partial c_4} = \frac{1}{2}c_3 + \frac{4}{5}c_4 - \frac{23}{60} \quad (2.98)$$

By setting these derivatives to zero, $c_3 = \frac{1}{2}$ and $c_4 = \frac{1}{6}$ can be computed. Here the trial functions employed were capable of representing the exact function, but this usually is impossible. In most situations, only approximate solutions can be achieved.

2.17 Luneburg Lens

A Luneburg lens is a spherically symmetric gradient-index lens, shown in Figure 2.12. A typical Luneburg lens's refractive index n decreases radially from the center to the outer

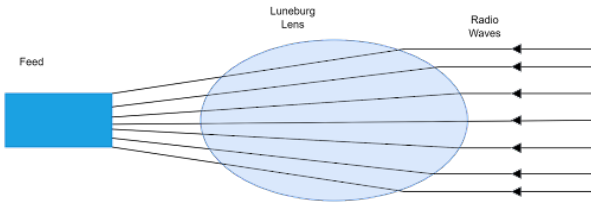


Fig. 2.12: Luneburg lens

surface. They can be made for use with electromagnetic radiation from visible light to radio waves.

Each point on the surface of an ideal Luneburg lens is the focal point for parallel radiation incident on the opposite side. Ideally, the dielectric constant ϵ_r of the material composing the lens falls from 2 at its center to 1 at its surface (or equivalently, the refractive index n falls from $\sqrt{2}$ to 1), derived from the equation below:

$$n = \sqrt{\epsilon_r} = \sqrt{2 - \left(\frac{r}{R}\right)^2} \quad (2.99)$$

Here R is the radius of the lens. Because the refractive index at the surface is the same as that of the surrounding medium, no reflection occurs at the surface. Within the lens, the paths of the rays are arcs of ellipses.

2.17.1 Uses in a microwave antenna

A Luneburg lens can be used as the basis of a high-gain radio antenna. This antenna is comparable to a dish antenna, but uses the lens rather than a parabolic reflector as the main focusing element. As with the dish antenna, a feed to the receiver or from the transmitter is placed at the focus, the feed typically consisting of a horn antenna. The phase centre of the feed horn must coincide with the point of focus, but since the phase centre is invariably somewhat inside the mouth of the horn, it cannot be brought right up against the surface of the lens. Consequently it is necessary to use a variety of Luneburg lens that focuses somewhat beyond its surface, rather than the classic lens with the focus lying on the surface. A variation on the Luneburg lens antenna is the hemispherical Luneburg lens antenna or Luneburg reflector antenna. This uses just one hemisphere of a Luneburg lens, with the cut surface of the sphere resting on a reflecting metal ground plane.

We apply the lens in our millimeter wave antenna setup to realize an antenna with higher resolution.

2.18 Summary

In this section we first reviewed Maxwell's equations.

This chapter introduces the basic theoretical knowledge of electromagnetism and antennas, the most important being Maxwell's equations, waveguides, horn antennas, antenna gain, impedance, the Friis equation, loss tangent, skin effect, Fresnel zone and cutoff frequency. These provide the theoretical basis for the design of the dielectric waveguide in this paper. Based on Maxwell's equations and the boundary conditions, the characteristics of the dielectric waveguide can be predicted. This can be simulated using the finite element method, where the basics stem out of the variational methods. The antenna can finally be tested, where the S-parameters play a big role in quantifying the performance.

Chapter 3

Qualitative Analysis of Dielectric Waveguide Antennas

In this chapter, we explain how the qualitative analysis of dielectric waveguide antennas was done. We first take a look at the tools we used for analysis and describe how we discovered the narrow beam being emitted from the tip of the dielectric waveguide.

3.1 Tools to Use

3.1.1 Vector network analyzers

A network analyzer is an instrument that measures the network parameters, mainly S-parameters, of electrical networks. Network analyzers are often used to characterize two-port networks such as amplifiers and filters, but they can be used on networks with an arbitrary number of ports. The vector network analyzer differs from the scalar network analyzer in the fact that the vector network analyzer measures both amplitude and phase properties.

A network analyzer, like most electronic instruments requires periodic calibration. There are several different methods of calibration.

- SOLT : an acronym for Short, Open, Load, Through, this is the simplest calibration method. As the name suggests, this requires access to known standards with a short circuit, open circuit, a precision load (usually 50 ohms) and a through connection. It is best if the test ports have the same type of connector (N, 3,5 mm etc.), but of a different gender. SOLT is suitable for coaxial measurements, where it is possible to obtain the short, open, load and through. The SOLT calibration method is less suitable for waveguide measurements, where it is difficult to obtain an open circuit or a load, or for measurements on non-coaxial test fixtures, where the same problems with finding suitable standards exist.

3.1. TOOLS TO USE



Fig. 3.1: MZ-mmcon1 in loopback mode



Fig. 3.2: Adalm Pluto

- TRL (through-reflect-line calibration): This technique is useful for microwave, non-coaxial environments such as fixture, wafer probing, or waveguide. TRL uses a transmission line, significantly longer in electrical length than the through line, of known length and impedance as one standard. TRL also requires a high-reflection standard (usually, a short or open) whose impedance does not have to be well characterized, but it must be electrically the same for both test ports.

3.1.2 MZ-mmCon1

MZ-mmCon1, shown in Figure 3.1, enables converting baseband signals of the 5 MHz to 6 GHz range up to the 27 GHz to 43 GHz range, and vice versa. It contains a 32 bit STM32F microcontroller containing both 12 bit analog to digital, digital to analog converters. The microcontroller also employs a wave table of maximum 4096 words with 2 channels, which can create and send constant wave signals. The microcontroller can also create arbitrary wave signals from data written in the flash memory. The device alone can produce constant wave and narrow band wave signals of under 100 kHz, and can modulate, demodulate, send, and receive millimeter wave signals. Upon receiving millimeter waves, the signal is demodulated and the baseband signal is converted to a digital signal, which can be analyzed on the computer by applying Fast Fourier Transformation (FFT). Figure 3.3 shows the FFT result visualized on the installed software.

3.1. TOOLS TO USE

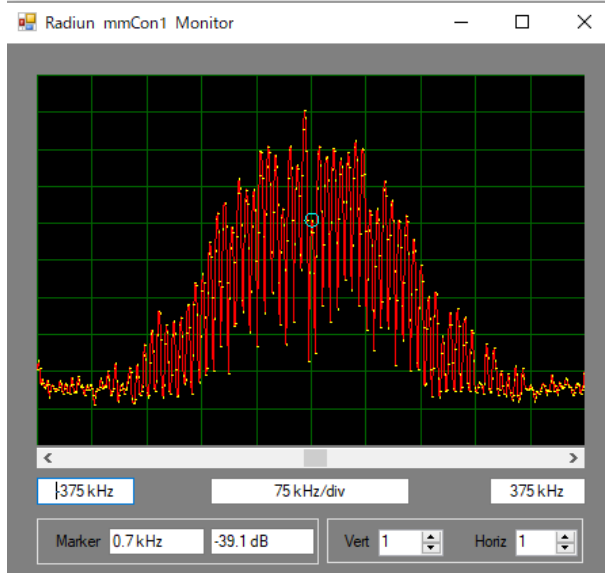


Fig. 3.3: FFT visualization on the software

3.1.3 MZ-mmAnt1

The MZ-mmAnt1 is a patch antenna designed for propagation of 28 GHz millimeter waves, with an antenna gain of roughly 5 dB. Using a SMPM to K connector adapter, the antenna can be hooked to the band pass filter and the up / down converter. The antenna can also be hooked up to a tripod by using the hole dug into the bottom of the structure.

3.1.4 Shield Box

A brass shield box was designed to emit the 60 GHz millimeter waves in a straightforward direction and prevent the waves from leaking out to other directions, as shown in Figure 3.6.

The VR-WH1 sender device was placed inside the box, as shown in 3.7.

3.1.5 Adalm Pluto

The ADALM-PLUTO Active Learning Module (PlutoSDR) is a tool available from Analog Devices Inc. (ADI) that can be used to simulate fundamental features of software-defined radio (SDR) or radio frequency (RF). The Communications Toolbox Support Package for Analog Devices ADALM-PLUTO Radio (PlutoSDR) enables the programmer to use MATLAB and Simulink to prototype, verify, and test practical wireless systems.

Here, the QPSK transmitter was implemented on Pluto to calculate the bit error rate in a 28GHz system. Bit error rate can be calculated as follows:

3.1. TOOLS TO USE



Fig. 3.4: mz-mmAnt1



Fig. 3.5: Waveguide to Coax Adapter



Fig. 3.6: Shield Box

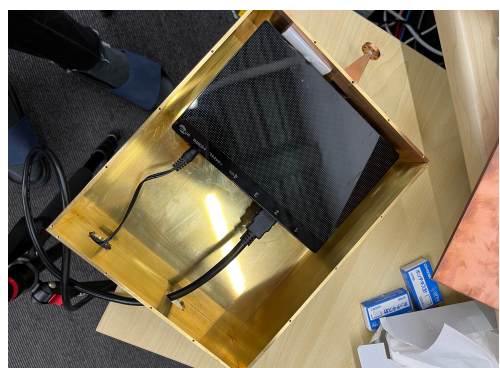


Fig. 3.7: VR-WH1 placed inside shield box

$$BER = \frac{\text{Number of error bits}}{\text{Number of total bits}} \quad (3.1)$$

3.1.6 Waveguide to Coax Adapter

For the 28 GHz system, we used the WR-28 UG-599/U square cover flange to 2.92mm female waveguide to coax adapter, which operates from 26.5 GHz to 40 GHz. The product ID of this adapter is PEWCA1078. This adapter offers a WR-28 waveguide interface size coupled with a precision tolerance UG-599/U flange. The PEWCA1078 is constructed of copper and plated in gold to ensure durability and repeatable RF performance.

3.1.7 Spectrum Analyzer

The Anritsu MS2762A spectrum analyzer was used for the 28 GHz system. Utilizing Anritsu's patented nonlinear transmission line (NLT) technology, it provides continuous coverage from 6 GHz to 170 GHz, with displayed average noise level (DANL) of -141/-136/-129/-122 dBm to 90/110/145/170 GHz, respectively. Powered by a USB type-C port, the spectrum can be analyzed on a Windows PC using the software provided by Anritsu. As the MS2762A port only supports the 0.8 mm connector, the following adapters were used to convert it to a K connector port (shown in Figure 3.8).

- 33W.8F50 (0.8 mm to W)
- 34WFV50 (W to V)
- 34VFKF50A (V to K)

3.2 Communication Medium Used in Embedded Systems

3.2.1 UART

UART, or universal asynchronous receiver-transmitter, is one of the most used device-to-device communication protocols. When properly configured, UART can work with many different types of serial protocols that involve transmitting and receiving serial data. In serial communication, data is transferred bit by bit using a single line or wire. In two-way communication, two wires are used for successful serial data transfer. Depending on the application and system requirements, serial communications needs less circuitry and wires, which reduces the cost of implementation. Here we explain the fundamental principles when using UART, with a focus on packet transmission and standard frame protocol.

3.2. COMMUNICATION MEDIUM USED IN EMBEDDED SYSTEMS

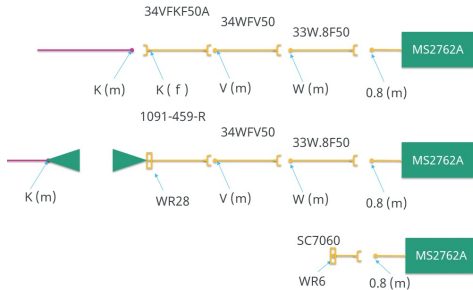


Fig. 3.8: Conversion of the port on MS2762A

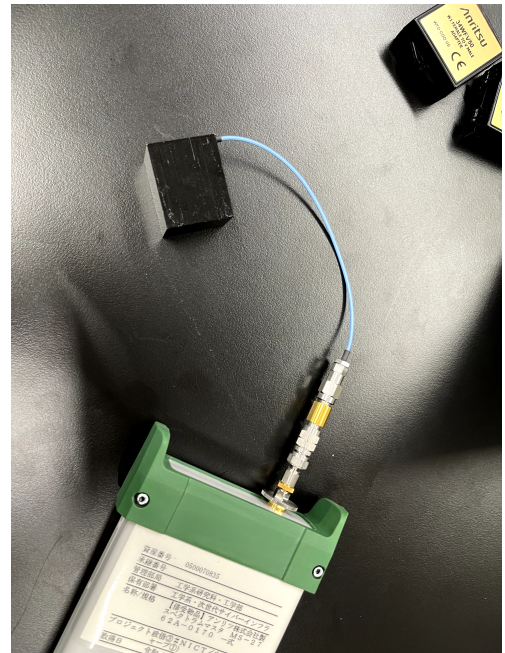


Fig. 3.9: The mz-mmAnt1 hooked up to the MS2762A

The image of the interface with data bus is shown in Figure 3.10.

The two signals of each UART device are named:

- Transmitter (Tx)
- Receiver (Rx)

The transmitting UART is connected to a controlling data bus that sends data in a parallel form. From this, the data will now be transmitted on the transmission line (wire)

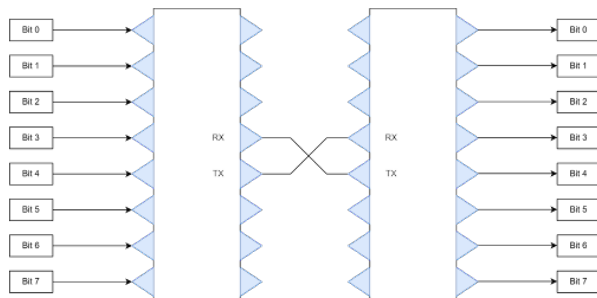


Fig. 3.10: UART with data bus



Fig. 3.11: UART packet

serially, bit by bit, to the receiving UART. This, in turn, will convert the serial data into parallel for the receiving device.

For UART and most serial communications, the baud rate needs to be set the same on both the transmitting and receiving device. The baud rate is the rate at which information is transferred to a communication channel. In the serial port context, the set baud rate will serve as the maximum number of bits per second to be transferred.

The UART interface does not use a clock signal to synchronize the transmitter and receiver devices; it transmits data asynchronously. Instead of a clock signal, the transmitter generates a bitstream based on its clock signal while the receiver is using its internal clock signal to sample the incoming data. The point of synchronization is managed by having the same baud rate on both devices. Failure to do so may affect the timing of sending and receiving data that can cause discrepancies during data handling. The allowable difference of baud rate is up to 10% before the timing of bits gets too far off. The image of the UART packet is shown in Figure 3.11:

3.2.2 SPI

Serial peripheral interface (SPI) is one of the most widely used interfaces between microcontroller and peripheral ICs such as sensors, ADCs, DACs, shift registers, SRAM, and others. SPI is a synchronous, full duplex main-subnode-based interface. The data from the main or the subnode is synchronized on the rising or falling clock edge. Both main and subnode can transmit data at the same time. The SPI interface can be either 3-wire or 4-wire. Here we focus on the popular 4-wire SPI interface.

4-wire SPI devices have four signals:

- Clock (SPI CLK, SCLK)
- Chip select (CS)
- main out, subnode in (MOSI)
- main in, subnode out (MISO)

The device that generates the clock signal is called the main. Data transmitted between the main and the subnode is synchronized to the clock generated by the main. SPI devices support much higher clock frequencies compared to I²C interfaces. SPI interfaces can have only one main and can have one or multiple subnodes. The chip select signal from the main is used to select the subnode. This is normally an active low signal and

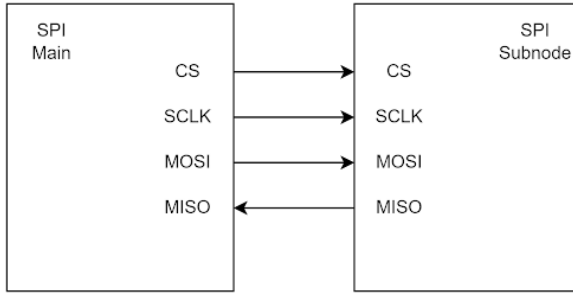


Fig. 3.12: SPI Communication

is pulled high to disconnect the subnode from the SPI bus. When multiple subnodes are used, an individual chip select signal for each subnode is required from the main. MOSI and MISO are the data lines. MOSI transmits data from the main to the subnode and MISO transmits data from the subnode to the main.

To begin SPI communication, the main must send the clock signal and select the subnode by enabling the CS signal. Usually chip select is an active low signal; hence, the main must send a logic 0 on this signal to select the subnode. SPI is a full-duplex interface; both main and subnode can send data at the same time via the MOSI and MISO lines respectively. During SPI communication, the data is simultaneously transmitted (shifted out serially onto the MOSI/SDO bus) and received (the data on the bus (MISO/SDI) is sampled or read in).

3.3 Qualitative Experiment with the Dielectric Waveguide

The authors constructed a 60GHz mmWave system to qualitatively analyze the characteristics of the PTFE waveguide. VR-WH1, a wireless HDMI transmission unit manufactured by Sharp, was used. Video was first streamed on a PC and transmitted via HDMI to the sender unit. The sender unit is enclosed in a brass box with a horn antenna attached to the front. The PTFE waveguide is attached to the horn antenna, which the authors held with their hands to control its beam emission direction. The receiver was placed a meter away from the waveguide tip, and the receiver was connected to an external monitor via HDMI. The authors also held a copper board between the sender and the receiver just in case of wave leakage.

When using the 60GHz mmWave system, the authors discovered that the PTFE waveguide emits a sharp beam from its tip, as shown in Figures 3.13 and 3.14. The video does not play (data is not received on the receiver) when the waveguide is not pointed to the receiver, and vice versa when pointed.

3.4. SUMMARY



Fig. 3.13: Video does not play (data is not received) when the waveguide is not pointed to the receiver



Fig. 3.14: Video plays when the waveguide is pointed to the receiver

3.4 Summary

In this chapter, we briefly explain how the qualitative analysis of dielectric waveguide antennas was done. We first take a look at the tools we used for analysis and describe how we discovered the narrow beam being emitted from the tip of the dielectric waveguide. This leads to the quantitative analysis of dielectric waveguide antennas in the next chapter.

Chapter 4

Quantitative Analysis of Dielectric Waveguide Antennas

4.0.1 Directivity Results

Working with NTT Docomo, the radiation patterns of the PTFE rod antenna were analyzed. The employed PTFE rod antenna had a diameter of 10 millimeters with a length of 20 centimeters. A PTFE rod antenna and the horn antenna were placed in an anechoic chamber with 1.2 meters in between.

The rod antenna was placed on a spinning platform , as shown in Figure 4.3 and 4.4. The PTFE rod antenna and the platform rotate in the anechoic chamber with the tip of the PTFE rod antenna at the center of the rotation.

The results are shown in Figures 4.5 and 4.6. The half power beamwidth was at around 20 degrees for both vertical and horizontal radiation patterns, and no significant difference was seen across all of the frequencies. There is a slight distortion in the data due to the PTFE rod antenna's slight change in its orientation while spinning.



Fig. 4.1: PTFE rod antenna with a diameter of 10 mm and length of 20 cm

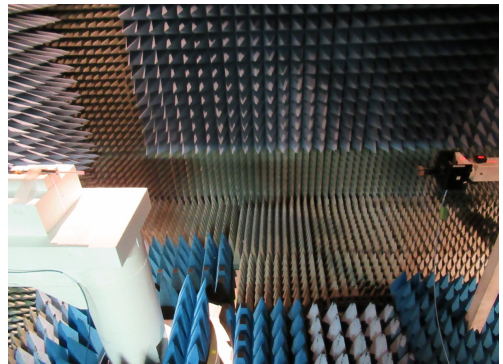


Fig. 4.2: Placement of antenna in anechoic chamber

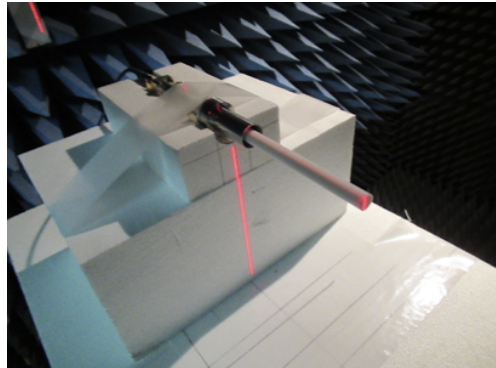


Fig. 4.3: PTFE rod antenna in anechoic chamber

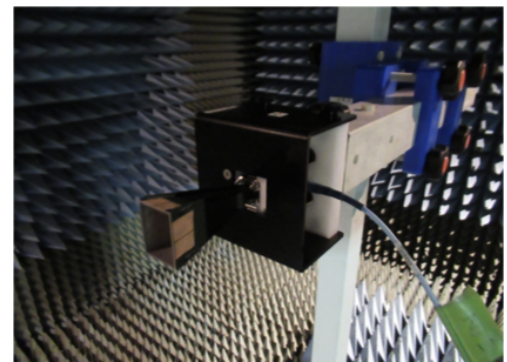


Fig. 4.4: Horn antenna in anechoic chamber

Comparison of Radiation Patterns in the Vertical Field from 27 GHz to 29 GHz

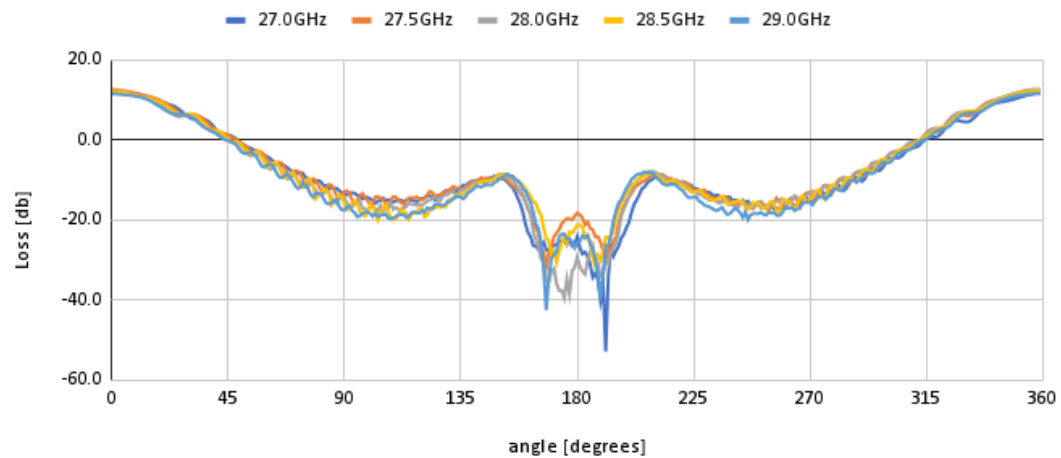


Fig. 4.5: Vertical Radiation Pattern

4.1. SUMMARY

Comparison of Radiation Patterns in the Horizontal Field from 27 GHz to 29 GHz

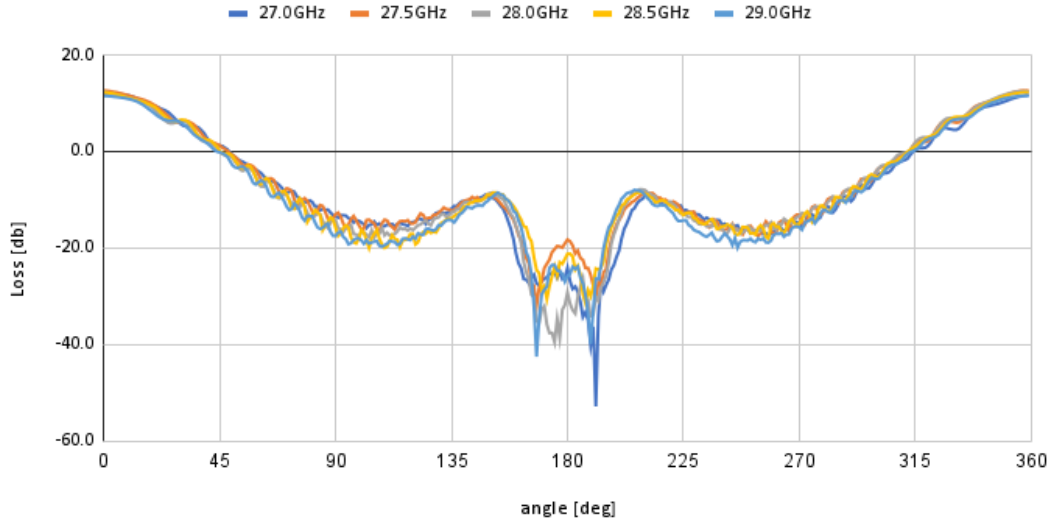


Fig. 4.6: Horizontal Radiation Pattern

4.1 Summary

Here we explained the actual experiment measuring the radiation pattern of the dielectric waveguide antenna. The radiation pattern showed that the dielectric waveguide antenna has the potential to create a high resolution beam, but still requires improvements. In the next chapter, we simulate different types of dielectric waveguides and see how the geometrical shape has an effect on space resolution.

Chapter 5

Dielectric Waveguide Antennas with Different Geometrical Tips

5.0.1 About the simulation conditions

Here we discuss the simulation conditions used in HFSS. As shown in Figure 5.1, HFSS with Hybrid and Arrays was employed for the solution type. By choosing network analysis, HFSS solves the design by exciting the ports individually and loading the remaining ports by matched characteristic impedances. The modal option enables HFSS to use electromagnetic power to solve the simulation problem.

A hybrid region is defined to enclose the model, and the type is specified as FE-BI (finite element boundary integral), as seen in Figure 5.2.

Two modes were designed for the wave port to excite the HFSS models. Both of them have integration lines defined, and modes are aligned analytically using the coordinate system. The two vectors representing the integration lines span the diameter of the wave port, and are placed in perpendicular fashion (Figure 5.3).

We chose the 58 GHz to 60 GHz for the solution setup of the simulation, with a step size of 1 GHz (Figure 5.4).

5.0.2 About the models

The models were all placed so that their radiation patterns were visualized on the x-y plane. 3 types of models were designed for the simulation as seen in Fig ??: dome, cone, and normal. Inspiration of the dome model comes from the Luneburg lens. The models are all set to a length of 50 millimeters and diameter of 10 millimeters, with each corresponding tip of optimized geometric shapes.

Directivity of the beam is the narrowest when using the dome shaped dielectric waveguide antenna. Next comes the normal antenna, and the cone shaped antenna, as shown in Fig. 5.8. The directivity of cone shaped antenna can be tuned by changing the length of the cone tip.

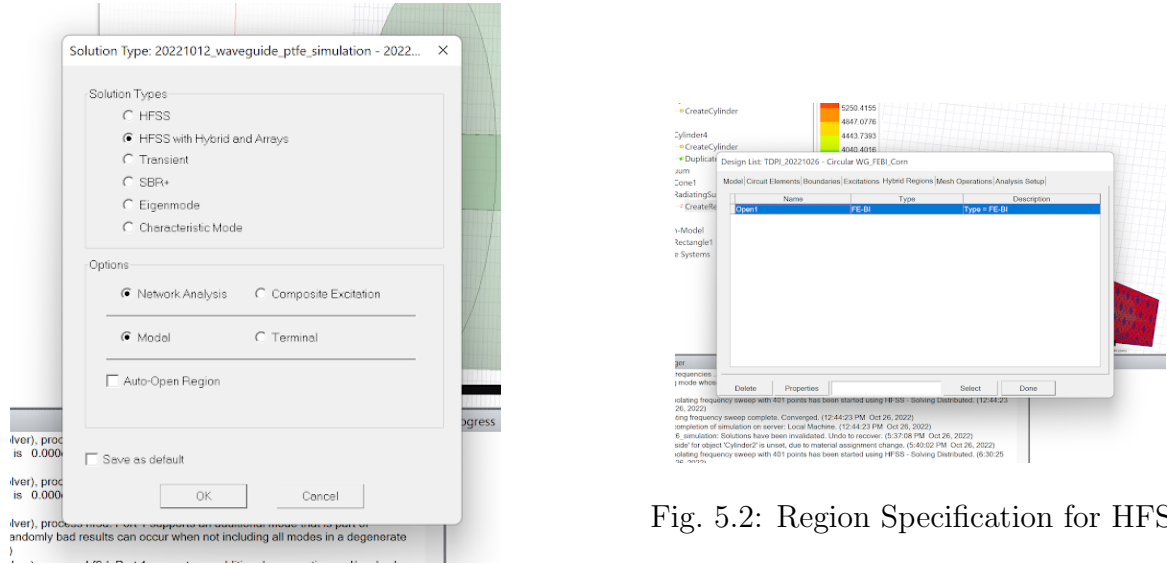


Fig. 5.1: Solution Type for HFSS

Fig. 5.2: Region Specification for HFSS

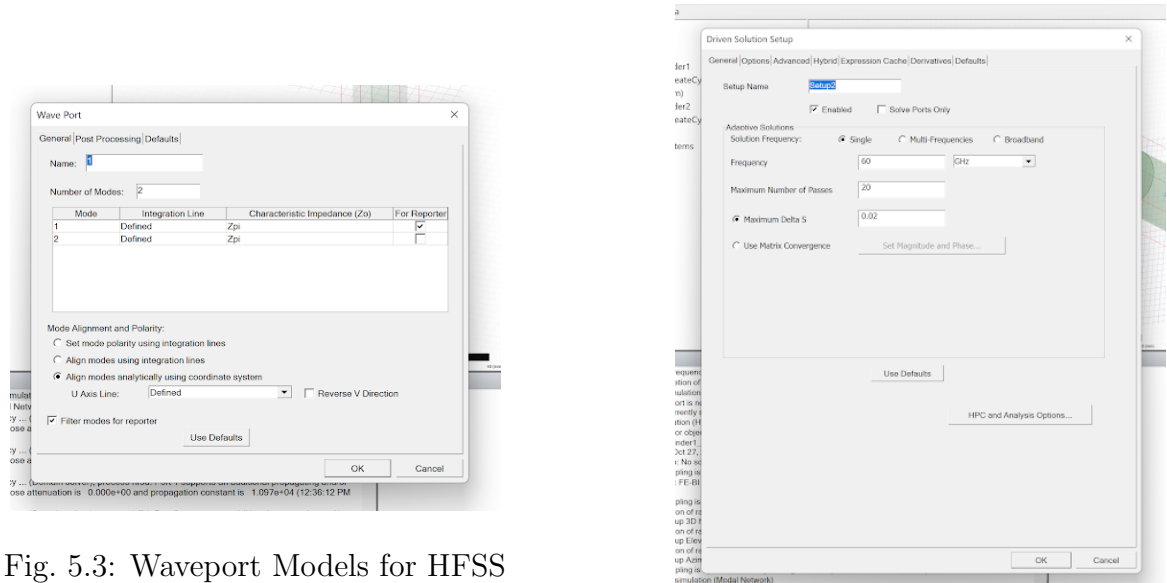


Fig. 5.3: Waveport Models for HFSS

Fig. 5.4: Solution Setup for HFSS

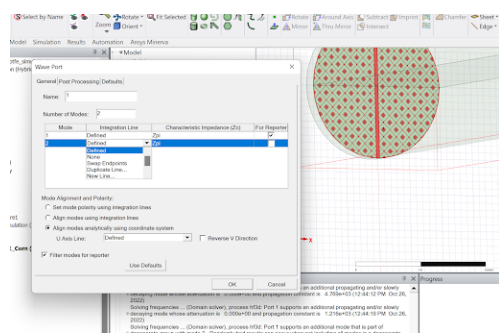


Fig. 5.5: Integration Line for HFSS

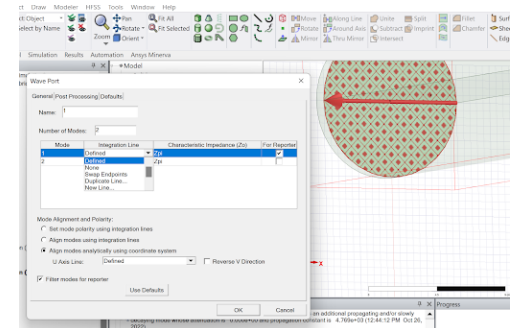


Fig. 5.6: Integration Line for HFSS for HFSS

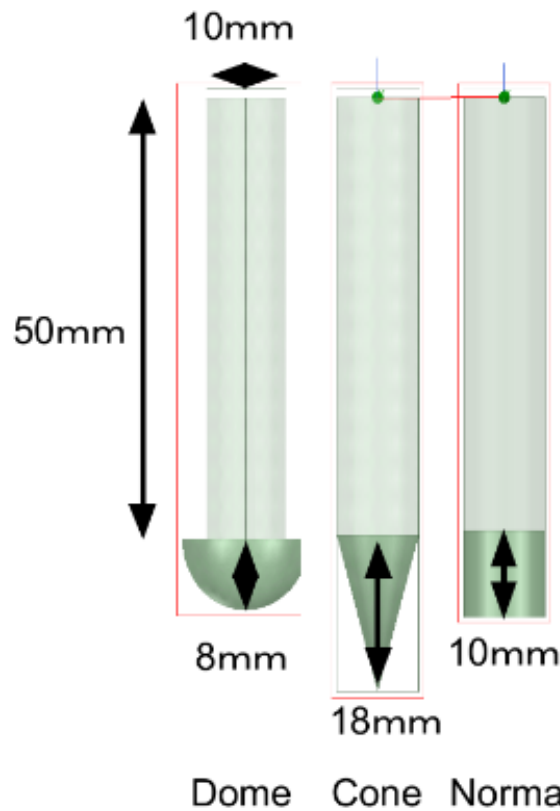


Fig. 5.7: HFSS simulation models

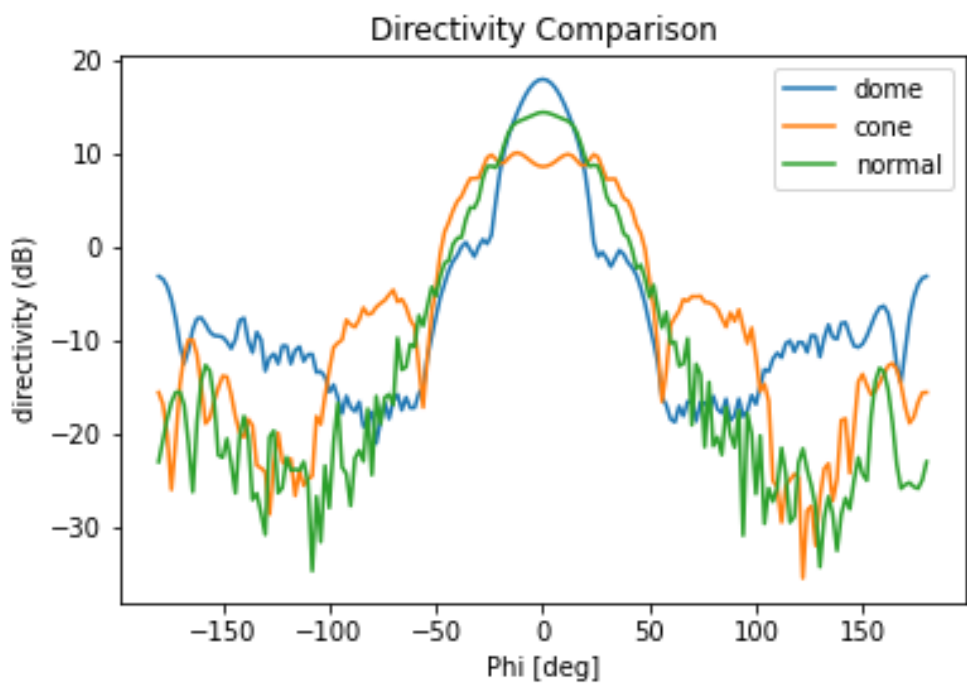


Fig. 5.8: HFSS simulation models

Dome: Half power beamwidth across different radii

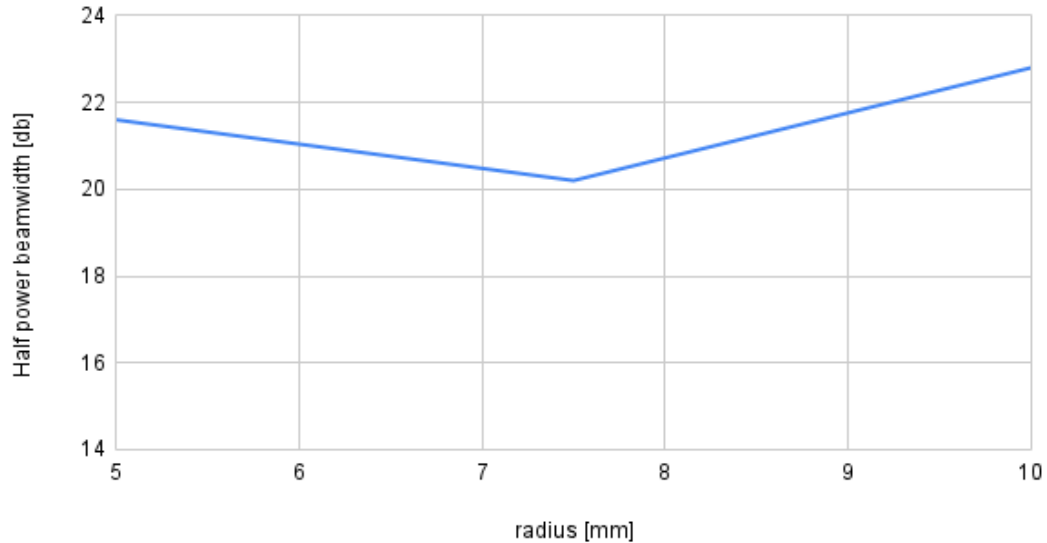


Fig. 5.9: Half power beamwidth of dome shaped antenna

Half power beamwidth of the dome shaped antenna was smallest at the radius of 7.5 millimeters to 8 millimeters, as shown in Fig. 5.9. The S11 parameter was also smallest at the radius of 7.5 millimeters to 8 millimeters.

5.0.3 S-parameter results from VNA based on simulation results

Based on the simulation results, a new dielectric waveguide was fabricated for the 28 GHz range. Using a PTFE dielectric waveguide with a diameter of 10 millimeters and length of 80 millimeters, the waveguide was sharpened to fit the coax-waveguide adapter with little to zero gap between the waveguide and the dielectric material, as shown in Fig. 5.11.

The S11 and S21 parameters were measured on the VNA. The signals were received using the mmAnt1 and the number of points was set to 1001. The frequency sweep was set to the range of 18 GHz to 30 GHz, and the IFBW is 1 kHz. The dielectric waveguide and the receiver antenna were placed in the same line with 0 degrees of insertion angle and distance of 10 cm.

The results are shown in Fig. 5.12 and 5.13. For S11 parameters, there is only -6 dB which is smaller compared to the simulation results. Also, the loss was smaller in the 28 GHz range compared to when having no dielectric waveguide, which is around -15 dB. This shows that the PTFE dielectric waveguide is contributing to less insertion loss.

For S21 parameters, the dielectric waveguide antenna again contributed to less loss, with a difference of about 10 dB at the same distance. Even when the distance was set

Dome: S params across different radii

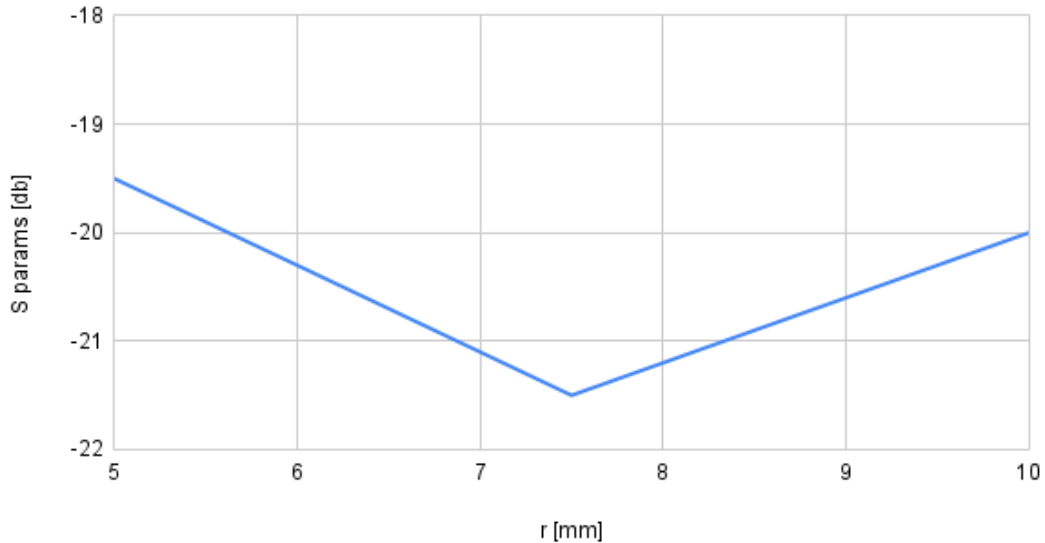


Fig. 5.10: S parameters of dome shaped antenna

to 20 cm, having the dielectric waveguide still resulted in less loss.

5.1 Summary

This chapter describes in detail the simulation and fabrication of the dielectric waveguide antenna. We first simulate three models with different geometrical tips attached and calculate their S-parameters and half power beamwidth on the simulation software. Next, we fabricate the dielectric waveguide antenna using a PTFE stick and measure the actual S-parameters and half power beamwidth using a network vector analyzer. The test results show that the dielectric waveguide antenna has less insertion loss and less propagation loss compared to when only using the metallic waveguide.

5.1. SUMMARY



Fig. 5.11: Dielectric waveguide fabricated for the 28 GHz range

5.1. SUMMARY

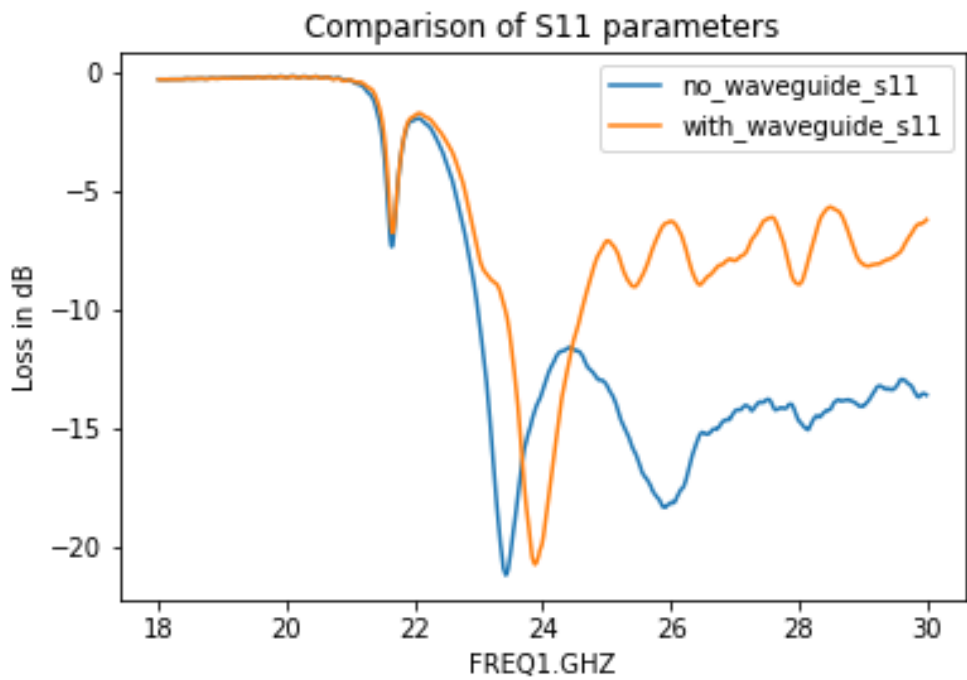


Fig. 5.12: Comparison of S11 parameters with dielectric waveguide and no waveguide

5.1. SUMMARY

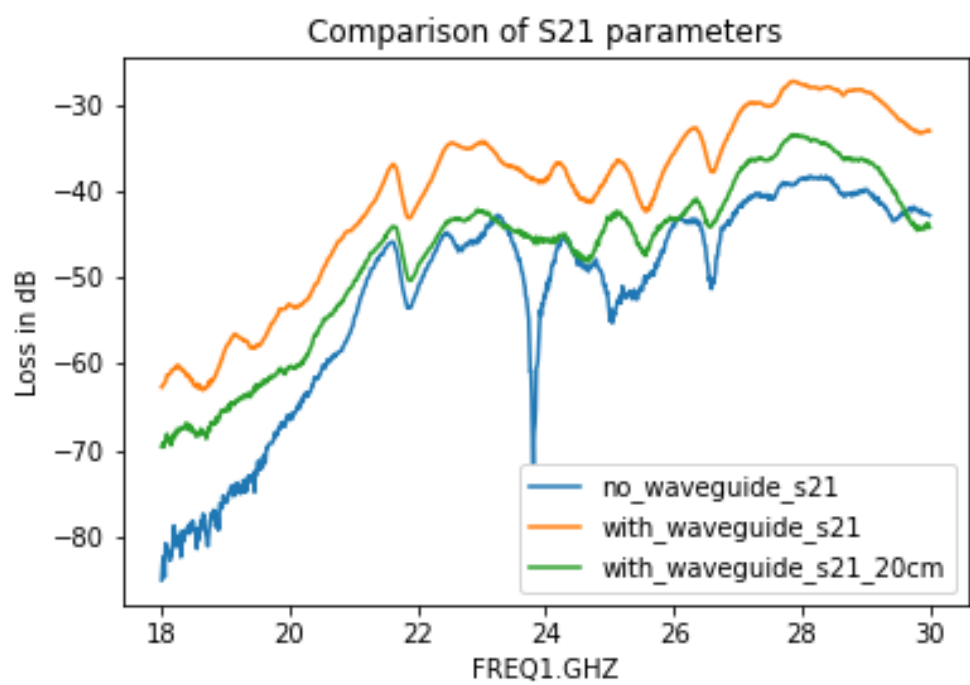


Fig. 5.13: Comparison of S21 parameters with dielectric waveguide and no waveguide

Chapter 6

Conclusion

In this paper, we presented a new method of implementing a dielectric waveguide antenna. After a detailed description of the electromagnetic and antenna principles, we detail the design and fabrication processes of the dielectric waveguide antennas. The antenna tests show that using a dielectric waveguide with tips of different geometrical shapes can satisfy the coverage requirements to some extent. Moreover, the waveguide antennas show some advantages for antenna manufacturing and network area construction.

We can draw the following conclusions based on the antenna design process, simulation results and testing results.

- As can be seen from the dielectric waveguide antennas designed, simulated and fabricated, the dielectric waveguide antennas, regardless of the geometrical shape of the tips, have certain suitability in terms of directivity. The total processing time and the raw materials required for processing are more favorable than the traditional processing methods. The size and internal design of the filter can also be freely designed and changed according to the design requirements. This will certainly be more convenient for the network users or antenna manufacturers.
- The use of dielectric waveguide antennas can contribute to create a new independent network area, which is beneficial in environments where there are clusters of devices in a small area. It also allows network engineers to add, modify and delete new network areas without affecting other networks in the environment.
- The accuracy of the sharpening process is essential for the production of the antenna. As antennas were manually sharpened in this study, there are minuscule errors in the structure of the dielectric waveguide. This alters the resolution and insertion loss of the antenna and requires recalibration of parameter measurements.

Chapter 7

Future Work

Based on the results of this work, it can be seen that the processing of antennas using dielectric material is an effective way to create a high resolution area. In this paper, only less than 10 structures have been designed and studied, and other more characteristic structures can be selected and explored in future studies. Furthermore, based on more superior modern antenna design principles, the antenna can be further optimized to have lower insertion loss without increasing its size.

In addition, there is a need to further improve the accuracy and the time required of the dielectric waveguide sharpening process. Sharpening the dielectric waveguide is harder for thinner and longer dielectric waveguide antennas. Hasty designs and implementation can result in less stable structure. Improving the sharpening process can allow the simulation results to better reflect the performance, thus making the simulation optimized dielectric waveguide antenna closer to the design requirements.

At the same time, the process of creating the correct waveguide adapter for the metallic waveguide and dielectric waveguide is also tricky. Our study did not create the adapter and resolved to sharpen the dielectric waveguide to have little to less gap in the aperture between the metallic and dielectric waveguide. The correct dimensions of both the metallic and dielectric waveguides must be carefully planned out to minimize the insertion loss. Therefore, this needs further research and exploration.

Our paper mainly focused on the rod antennas created with dielectric materials. One of the structures we did not try in this paper was using a dielectric sheet to create a mmWave network area. Using a two dimensional sheet can also provide a variety of usecases and can have contributions in ways that a rod antenna cannot. There have been studies done on lower frequencies in the past [33].

Finally, using 3D printing technology to create the geometrical shape of the rod antenna may also prove to be effective. The geometrical structure of the antenna tip can be increased in complexity accordingly, as long as it meets the processing requirements of the 3D printer. This can enable much shorter lead times and less manual manufacturing work.

Bibliography

- [1] Robert Pepper. Cisco visual networking index (vni) global mobile data traffic forecast update. *Technical report, Cisco, Tech. Rep.*, 2013.
- [2] INC. NTT DOCOMO. Docomo 6g white paper. 2014.
- [3] Ki Young Kim, Jong Ryul Sohn, Hyun Ju Seo, Jin-Won Han, Heung-Sik Tae, and Jeong-Hae Lee. Radiation characteristics of flexible circular dielectric waveguides in q-band. In *IEEE Antennas and Propagation Society International Symposium (IEEE Cat. No.02CH37313)*, Vol. 4, pp. 440–443 vol.4, 2002.
- [4] Hirosuke Suzuki and Kenji Saito. Moving target using dielectric waveguide for radar-based pre-crash safety systems. *2013 European Radar Conference*, pp. 220–222, 2013.
- [5] Theodore S. Rappaport, Shu Sun, Rimma Mayzus, Hang Zhao, Yaniv Azar, Kevin Wang, George N. Wong, Jocelyn K. Schulz, Mathew Samimi, and Felix Gutierrez. Millimeter wave mobile communications for 5g cellular: It will work! *IEEE Access*, Vol. 1, pp. 335–349, 2013.
- [6] Atsushi Fukuda, Hiroshi Okazaki, and Shoichi Narahashi. A novel beam control method and configuration for phased array antenna system employing frequency-upconverted local signals with phase difference. In *2016 IEEE Radio and Wireless Symposium (RWS)*, pp. 36–38, 2016.
- [7] Yudai Shigeta, Keita Kitagawa, Atsushi Sanada, Atsushi Fukuda, Kunihiro Kawai, and Hiroshi Okazaki. A 28 ghz interleaved circular antenna array with equal gains and wideband orthogonality for analog oam multiplexing. In *2019 IEEE Asia-Pacific Microwave Conference (APMC)*, pp. 1008–1010, 2019.
- [8] Atsushi Fukuda, Hiroshi Okazaki, and Shoichi Narahashi. A phased array antenna system employing frequency-upconverted local signals with phase difference. In *2015 IEEE International Symposium on Radio-Frequency Integration Technology (RFIT)*, pp. 202–204, 2015.
- [9] Atsushi Fukuda, Hiroshi Okazaki, and Shoichi Narahashi. A broadband phased-array antenna system employing frequency-upconverted local signals with phase difference.

BIBLIOGRAPHY

- IEEE Transactions on Microwave Theory and Techniques*, Vol. 67, No. 1, pp. 383–391, 2019.
- [10] Baolin Cao, Hao Wang, and Yong Huang. W-band high-gain te₂₂₀-mode slot antenna array with gap waveguide feeding network. *IEEE Antennas and Wireless Propagation Letters*, Vol. 15, pp. 988–991, 2016.
 - [11] Milad Sharifi Sorkherizi, Abdolmehdi Dadgarpour, and Ahmed A. Kishk. Planar high-efficiency antenna array using new printed ridge gap waveguide technology. *IEEE Transactions on Antennas and Propagation*, Vol. 65, No. 7, pp. 3772–3776, 2017.
 - [12] Yan Ding and Ke Wu. A 4 × 4 ridge substrate integrated waveguide (rsiw) slot array antenna. *IEEE Antennas and Wireless Propagation Letters*, Vol. 8, pp. 561–564, 2009.
 - [13] Xiao-Ping Chen, Ke Wu, Liang Han, and Fanfan He. Low-cost high gain planar antenna array for 60-ghz band applications. *IEEE Transactions on Antennas and Propagation*, Vol. 58, No. 6, pp. 2126–2129, 2010.
 - [14] Jie Wu, Yu Jian Cheng, and Yong Fan. A wideband high-gain high-efficiency hybrid integrated plate array antenna for v-band inter-satellite links. *IEEE Transactions on Antennas and Propagation*, Vol. 63, No. 4, pp. 1225–1233, 2015.
 - [15] Seyed Ali Razavi, Per-Simon Kildal, Liangliang Xiang, EsperanzaAlfonso Al 坦 s, Haiguang Chen. 2× 2-slot element for 60-ghz planar array antenna realized on two doubled-sided pcbs using siw cavity and ebg-type soft surface fed by microstrip-ridge gap waveguide. *IEEE Transactions on Antennas and Propagation*, Vol. 62, No. 9, pp. 4564–4573, 2014.
 - [16] Jinlin Liu, Abbas Vosoogh, Ashraf Uz Zaman, and Jian Yang. A slot array antenna with single-layered corporate-feed based on ridge gap waveguide in the 60 ghz band. *IEEE Transactions on Antennas and Propagation*, Vol. 67, No. 3, pp. 1650–1658, 2019.
 - [17] Abbas Vosoogh, Milad Sharifi Sorkherizi, Vessen Vassilev, Ashraf Uz Zaman, Zhongxia Simon He, Jian Yang, Ahmed A. Kishk, and Herbert Zirath. Compact integrated full-duplex gap waveguide-based radio front end for multi-gbit/s point-to-point backhaul links at e-band. *IEEE Transactions on Microwave Theory and Techniques*, Vol. 67, No. 9, pp. 3783–3797, 2019.
 - [18] Yaser S. E. Abdo, M. R. Chaharmir, J. Shaker, and Y. M. M. Antar. Investigation of the transition between two different ebg waveguides. *IEEE Antennas and Wireless Propagation Letters*, Vol. 9, pp. 1002–1005, 2010.

BIBLIOGRAPHY

- [19] Elena Pucci, Eva Rajo-Iglesias, and Per-Simon Kildal. New microstrip gap waveguide on mushroom-type ebg for packaging of microwave components. *IEEE Microwave and Wireless Components Letters*, Vol. 22, No. 3, pp. 129–131, 2012.
- [20] Mahsa Ebrahimpouri, Oscar Quevedo-Teruel, and Eva Rajo-Iglesias. Design guidelines for gap waveguide technology based on glide-symmetric holey structures. *IEEE Microwave and Wireless Components Letters*, Vol. 27, No. 6, pp. 542–544, 2017.
- [21] Eva Rajo-Iglesias, Mahsa Ebrahimpouri, and Oscar Quevedo-Teruel. Wideband phase shifter in groove gap waveguide technology implemented with glide-symmetric holey ebg. *IEEE Microwave and Wireless Components Letters*, Vol. 28, No. 6, pp. 476–478, 2018.
- [22] Abbas Vosoogh, Herbert Zirath, and Zhongxia Simon He. Novel air-filled waveguide transmission line based on multilayer thin metal plates. *IEEE Transactions on Terahertz Science and Technology*, Vol. 9, No. 3, pp. 282–290, 2019.
- [23] Yohei Miura, Jiro Hirokawa, Makoto Ando, Yuzo Shibuya, and Goro Yoshida. Double-layer full-corporate-feed hollow-waveguide slot array antenna in the 60-ghz band. *IEEE Transactions on Antennas and Propagation*, Vol. 59, No. 8, pp. 2844–2851, 2011.
- [24] Abbas Vosoogh, Per-Simon Kildal, and Vessen Vassilev. Wideband and high-gain corporate-fed gap waveguide slot array antenna with etsi class ii radiation pattern in v -band. *IEEE Transactions on Antennas and Propagation*, Vol. 65, No. 4, pp. 1823–1831, 2017.
- [25] Jiro Hirokawa, Miao Zhang, and Makoto Ando. 94ghz fabrication of a slotted waveguide array antenna by diffusion bonding of laminated thin plates. In *SENSORS, 2009 IEEE*, pp. 907–911, 2009.
- [26] Miao Zhang, Jiro Hirokawa, and Makoto Ando. An e-band partially corporate feed uniform slot array with laminated quasi double-layer waveguide and virtual pmc terminations. *IEEE Transactions on Antennas and Propagation*, Vol. 59, No. 5, pp. 1521–1527, 2011.
- [27] Cheng Jin, Jianhong Chen, Binchao Zhang, Lingwen Kong, Sining An, Zhongxia Simon He, and Jinlin Liu. Low-cost mmwave metallic waveguide based on multilayer integrated vertical-ebg structure and its application to slot array antenna design. *IEEE Transactions on Antennas and Propagation*, Vol. 70, No. 3, pp. 2205–2213, 2022.
- [28] Kunihiro Kawai, Takuma Takada, Atsushi Fukuda, Hiroshi Okazaki, and Shoichi Narahashi. A new area formation approach for millimeter wave communication systems employing a dielectric waveguide. In *2015 European Microwave Conference (EuMC)*, pp. 1088–1091, 2015.

BIBLIOGRAPHY

- [29] Atsushi Fukuda, Kunihiro Kawai, Hiroshi Okazaki, and Yasunori Suzuki. Experimental study of leaky-wave antenna employing bent dielectric waveguide for millimeter wave communication. In *2020 IEEE International Symposium on Radio-Frequency Integration Technology (RFIT)*, pp. 199–201, 2020.
- [30] Michael Meurer and Felix Antreich. *Springer Handbook of Global Navigation Satellite Systems - Signals and Modulation*, pp. 91–119. 2017.
- [31] K. Kurokawa. Power waves and the scattering matrix. *IEEE Transactions on Microwave Theory and Techniques*, Vol. 13, No. 2, pp. 194–202, 1965.
- [32] Jianming Jin. *The Finite Element Method in Electromagnetics*. Wiley-IEEE Press, 3rd edition, 2014.
- [33] Hiroyuki Shinoda, Yasutoshi Makino, Naoshi Yamahira, and Hiroto Itai. Surface sensor network using inductive signal transmission layer. In *2007 Fourth International Conference on Networked Sensing Systems*, pp. 201–206, 2007.